MULTIFUNCTIONAL OPTICAL SIGNAL-PROCESSING
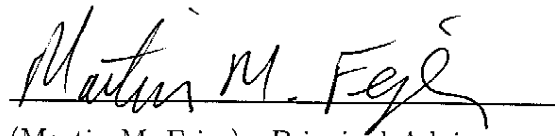DEVICES IN PERIODICALLY POLED LITHIUM NIOBATE

A DISSERTATION
SUBMITTED TO THE DEPARTMENT OF APPLIED PHYSICS
AND THE COMMITTEE ON GRADUATE STUDIES
OF STANFORD UNIVERSITY
IN PARTIAL FULFILLMENT OF THE REQUIREMENTS
FOR THE DEGREE OF
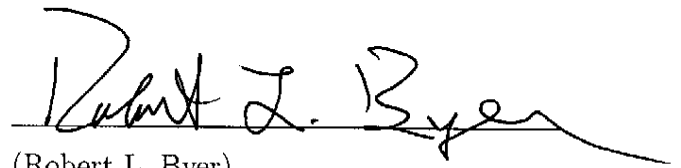DOCTOR OF PHILOSOPHY

Jie Huang
June 2007

I certify that I have read this dissertation and that, in my opinion, it is fully adequate in scope and quality as a dissertation for the degree of Doctor of Philosophy.

(Martin M. Fejer)   Principal Adviser

I certify that I have read this dissertation and that, in my opinion, it is fully adequate in scope and quality as a dissertation for the degree of Doctor of Philosophy.
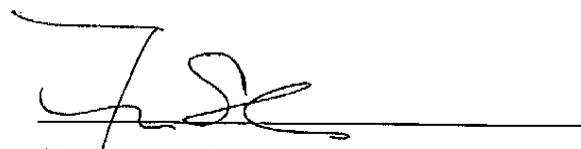
(Robert L. Byer)

I certify that I have read this dissertation and that, in my opinion, it is fully adequate in scope and quality as a dissertation for the degree of Doctor of Philosophy.

(Shanhui Fan)

Approved for the University Committee on Graduate Studies.

iii

Abstract

Optical signal processing is becoming an attractive technology for communication applications. Many important optical signal-processing functions have been demonstrated in devices based on periodically poled lithium niobate (PPLN) waveguides. They are among the fastest and most efficient nonlinear optical devices available today.

The work described in this dissertation further extends the functionality of PPLN optical signal processors by lifting two limitations long imposed on such devices: A broadband quasi-group-velocity-matched scheme is invented to obviate the bandwidth-efficiency trade-off inherent in optical frequency mixers, and several techniques are developed to modulate the nonlinear interaction amplitude and thereby versatilely shape the transfer function of an optical signal processor.

The ability of optical signal processors to process high speed data beyond what is possible with electronics has been applied to optical time-division multiplexing (OTDM), a technique complementary to wavelength-division multiplexing. In this dissertation, multiple functions are tailored and monolithically integrated to make a PPLN-based optical time-division multiplexer (OTDM-MUX) capable of 160-Gbit/s operation. It is successfully characterized using ultrafast optical techniques. Compared with previously demonstrated OTDM-MUXs, besides the advantages of a monolithic layout, the PPLN MUX has higher efficiency while keeping the crosstalk low.

Beyond discrete functions, engineered nonlinear optical and optical circuit components have opened the door to a new level of versatility of PPLN-based optical signal-processing devices.

Acknowledgments

My endeavors, in and beyond this dissertation, would not have been successful without the support of my colleagues, friends, and family. Luck plays a remarkably important role for me to be surrounded by many extraordinary people during my Stanford years.

One could hardly hope for a better advisor than Professor Martin M. Fejer. Marty sets a high standard for his research group, and is supportive of his students in every possible way. Whenever I had a problem in research and went to Marty, without fail he was able to show me the way forward. When I listened to him, the solution would always work – obviously I haven't always listened to him, otherwise I could have done much more. Marty's dedication to research and the breadth and depth of his knowledge on all things scientific have greatly amazed me and others in his group – if that is what it takes to excel in scientific research, many have followed this role model and become good scientists, while I am scared away to do something easier. I greatly appreciate the freedom Marty gives us to make plans, to use our time, and to pursue other important things in life.

I thank Professors Robert Byer and Shanhui Fan for their time spent and valuable comments on this work. Professor Byer's enthusiasm and positive thinking have inspired me. I not only learned sciences from him, but also enjoyed the beautiful photographs of galaxies he took in Hawaii, as well as the interesting and insightful stories of this university and American higher education. Professor Fan taught me the theory of guided-wave optics in the classroom, and after reading this dissertation everyone can see how indispensable that piece of knowledge is to my work.

I have been privileged to work with many talented and generous people. Jonathan Kurz passed to me a great deal of hands-on knowledge of nonlinear optics experiments,

and part of my research was the natural extension of his. Xiuping Xie and I collaborated in a number of projects; be it theory, experiments, coding, or moving, his help to me was all over the place. Carsten Langrock built some important apparatus that I used from my second year through my sixth year. It was also he who persuaded and taught me to use LaTeX, in no small part important to this work. Rosti Roussev's waveguide model has been the foundation of much going on in this group. David Hum helped me to solve many of the nonlinear optics problems. I also have had the pleasure to work with Mathieu Charbonneau-Lefort, Paulina Kuo, Joe Schaar, Andy Schober, and Scott Sifferman on a day-to-day basis. Many other Byer-Fejer group students and visiting scholars have contributed to my research, through discussions, by helping me locate a piece of equipment, or, like Gennady Imeshev, by having written a thorough dissertation that I repeatedly resorted to in the writing of this one.

Many thanks to Tom Carver, Tim Brand, and Paul Jerabek for their help in fabricating PPLN devices, to Dr. Roger Route for his continuous effort to make sure I got paid on the correct account for the correct amount, and to Paula Perron, Claire Nicholas, and Vivien Drew for making this department and this group such a pleasant place.

I am grateful to my friends. Near and far, they have always been important to me.

Without my parents and grandparents, I would not be the person I am today. I thank them for their unconditional love and support. Finally, my wife Ines. As little as she knows about nonlinear optics, she has never doubted the value of a Ph.D. degree, even alleging that she may want one herself after getting a J.D. – that was comforting during the days when nothing in the lab seemed to work the way it should. I thank her for being my last resort, and for loving me no matter what.

Contents

List of Tables

List of Figures

xiv

Chapter 1

Introduction

1.1 Overview

The explosive growth in data traffic strongly motivates more efficient and economical utilization of the bandwidth of fiber-optic networks. The transmission and management of high capacity data is creating enormous demands for components with signal-processing capabilities beyond those currently available. While optoelectronic components (with speed limitation of 40 Gbit/s currently) will remain important in the future, all-optical techniques may be useful to fully exploit the transmission bandwidth of optical fibers (exceeding 3 Tbit/s) to allow for new services such as digital television and the next-generation Internet. [1] All-optical signal processing replaces high-speed electronics with all-optical components and makes the signal conversions between the optical and electrical domain unnecessary. Optical signal processors based on periodically poled lithium niobate (PPLN) have the advantages of high efficiency (>3000%/W), high speed (>1 THz of modulation bandwidth), preservation of phase information, large wavelength-conversion bandwidth (> 70 nm), large dynamic range (>50 dB), and quantum-limited spontaneous emmision (parametric fluorescence) noise. [2]

At the center of optical signal-processing devices is an optical frequency (OF) mixer, an optical analogue of the radio-frequency (RF) mixers commonly used in electronics. (Figure 1.1) OF mixers produce a frequency-shifted output by mixing
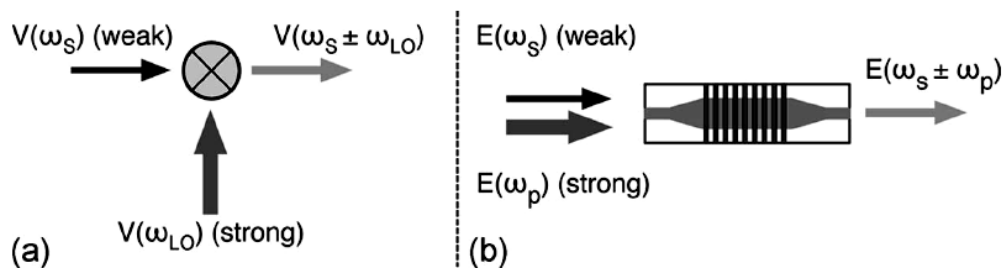
Figure 1.1: (a) Radio frequency mixer and (b) optical frequency mixer. In both mixers, the output is generated through frequency mixing of the signal and a local oscillator. (Adapted from Ref. [4].)
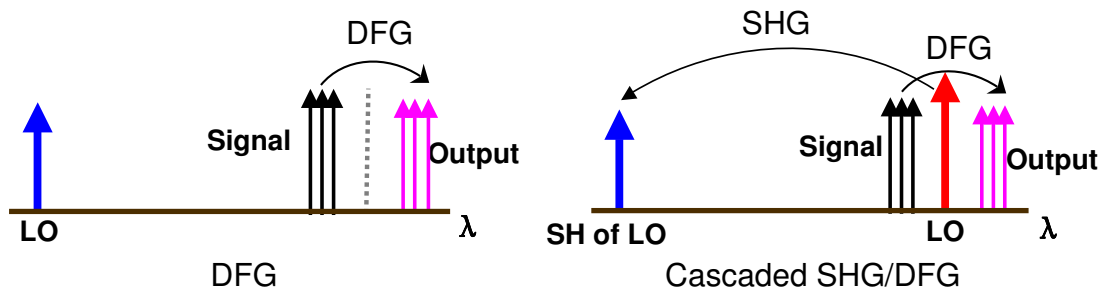
Figure 1.2: Nonlinear optical processes in an OF mixer. Left: the output is the difference frequency between the local oscillator and signal; right: cascaded SHG/DFG, the signal mixes with frequency-doubled local oscillator through DFG.

the input signal with a local oscillator. Standard OF mixers are based on difference-frequency generation (DFG) of a first-harmonic (FH) signal (around 1550 nm) and a second-harmonic (SH) local oscillator (around 775 nm), or on cascaded second-harmonic-generation(SHG)/DFG where the SH of a 1.5-μm local oscillator is the pump of the DFG. [3] (Figure 1.2)

During a decade of development, a variety of signal-processing functions have been demonstrated using OF mixers based on PPLN waveguides. [4] To name a few, signal manipulations such as wavelength conversion, [5, 6, 7] phase conjugation, [8, 9] pulse shaping, [10] optical sampling, [11, 12] gated mixing, [13] time-slot interchange, [14] and header recognition [15] can now be performed in the optical domain.

Notwithstanding all these exciting developments, two constraints have long limited the application of PPLN optical signal-processing devices:

The bandwidth/efficiency trade-off

On the one hand, the efficiency of an OF mixer is proportional to the square (for single step process) or the fourth power (for cascaded processes) of the interaction length, L. [6] On the other hand, while the signal bandwidth for a typical configuration is broader than the bandwidth of an Erbium-doped fiber amplifier (EDFA), [4] the local oscillator (pump) bandwidth is limited by the group-velocity mismatch (GVM) between the interacting FH and SH waves. The slower SH pump pulse walks off the FH pulse that it is supposed to interact with. In other devices where SHG is involved (a cascaded OF mixer for example), the generated SH pulse is broadened due to its smaller group velocity and eventually becomes incompatible with the system's bit rate. (Figure 1.3) In either case, the pump bandwidth of the device scales inversely with L. The group-delay difference between FH and SH of a typical 5-cm-long PPLN device is approximately 18 ps, while one time slot in a 160-Gbit/s system is only 6.25 ps and the pulse width is usually even shorter. In order to allow for high bit rate, one needs to use a short device and hence sacrifice efficiency. This bandwidth/efficiency trade-off is inherent in optical signal-processing devices based on parametric interactions.

In Chapter 2, we mitigate this trade-off with a quasi-group-velocity-matched
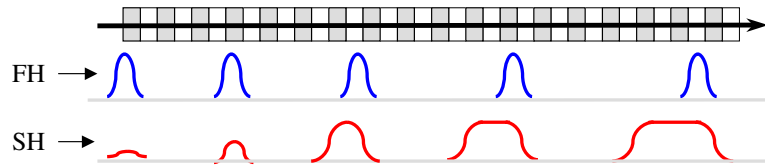
Figure 1.3: Group-velocity mismatch between the FH and SH light. The SH lags the FH as it is generated, becoming a broadened pulse.

(QGVM) structure. It is a demonstration of how waveguide-based integrated-optic structures can extend the functionality of optical signal-processing devices.

Fixed nonlinear interaction amplitude

In digital signal processing, a window function can be conveniently applied to alter the signal spectrum. For an OF mixer, however, the frequency-domain response (transfer function) is largely determined by material dispersion: a rectangular window function and hence a sinc transfer function is intrinsic to a device with a uniform nonlinear response along its entire length. The relatively large and slowly-decaying sidelobes of a sinc curve can cause crosstalk in some applications. (Figure 1.4) Until recently, a technique to versatilely shape the transfer function has not been available.
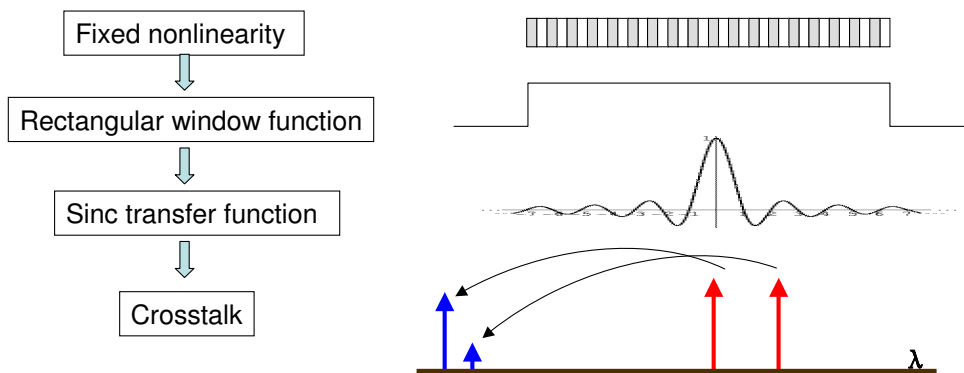
Figure 1.4: A uniform QPM grating has an intrinsic sinc transfer function, causing crosstalk in frequency conversion.

The root of the difficulty lies in the physics of OF mixers. The frequency-domain

response is determined by the Fourier transform of the spatial distribution of nonlinear interaction amplitude. With the quasi-phasematching (QPM) technique, the local nonlinear coefficient takes the material value with either a plus or a minus sign: any value in between those limits is not readily available. A technique to obtain continuously adjustable local nonlinear interaction amplitude is the key to shaping the transfer function.

The ability to shape the transfer function is essential in optical signal processing, as many signal-processing functions depend on the ability to alter the signal spectrum in a controlled way: arbitrary spectral shaping enables many more signal-processing possibilities. In Chapter 3 we develop several techniques to modulate the local amplitude of nonlinear interactions, and experimentally prove their effectiveness in one specific application that is important in optical communications – suppressing the transfer function sidelobes to minimize interchannel crosstalk. With this we demonstrate how QPM engineering has opened the door to a new level of versatility of optical signal-processing devices.

The transfer function is so fundamental in optical signal processing that its distortion due to fabrication errors calls for further study. In Appendix A we present an analytical study of the tuning behavior of QPM devices in the context of non-ideal waveguides. Together with Ref. [16], which treated QPM domain errors, the results constitute a complete error analysis of waveguide-based QPM devices. They are useful to establish fabrication tolerances in practical applications and as diagnostic tools for analyzing experimental results.

The ability of optical signal processors to process high speed data has been applied to optical time-division multiplexing (OTDM), a technique that is complementary to wavelength-division multiplexing (WDM). In an OTDM system, multiple channels at low bit rate are multiplexed into a high-bit-rate stream where pulses from different channels occupy different time slots. (Figure 1.5) By combining WDM and OTDM, point-to-point optical links with data capacities close to the theoretical maximum can be designed. Furthermore, OTDM systems have several advantages over WDM systems such as high bit-rate-to-bandwidth ratio, natural accommodation of higher
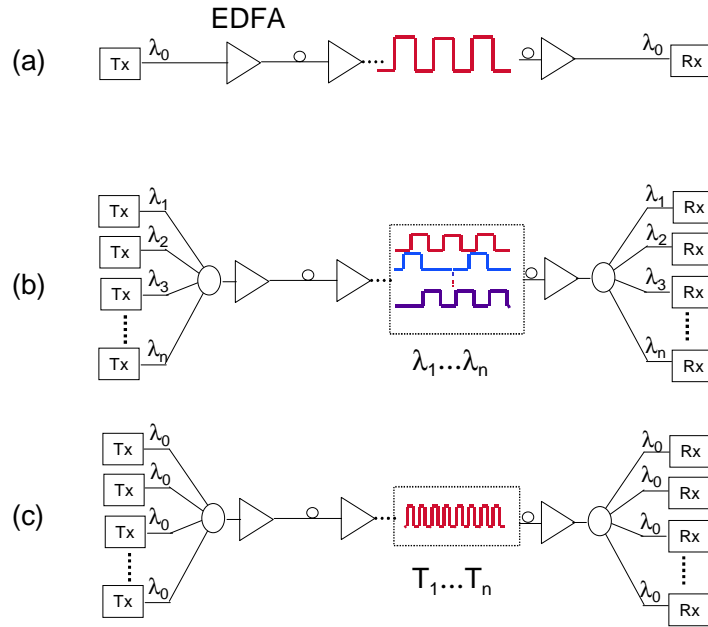
Figure 1.5: Optical fiber transmission systems: (a) single channel; (b) WDM; (c) TDM. (Adapted from Ref. [3].)

bit-rate payloads, and ease of supervising the multiplexed line. [17]

Key to an OTDM system is an OTDM multiplexer (MUX) that produces stable time-sequential signals from multiple data channels. All-optical 160-Gbit/s OTDM-MUXs were previously demonstrated using PPLN waveguides integrated with a planar lightwave circuit (PLC). [18, 19] The hybrid scheme integrated on one PPLN chip and two PLC chips a number of PPLN and silica-on-silicon waveguides, and used a topology where most of the light was wasted in the couplers. In Chapter 4, we describe a monolithic MUX capable of 160-Gbit/s operation fabricated entirely on a single PPLN substrate. By tailoring and integrating multiple optical signal-processing functions, we are able to build a MUX using one PPLN waveguide without the additional silica-on-silicon circuitry, hence achieving a simpler and monolithic layout and higher efficiency while keeping crosstalk low. This is arguably one of the more sophisticated all-optical signal-processing devices ever demonstrated. It exemplifies the integrated operation of optical signal processing in PPLN beyond simple discrete functions.

This dissertation is built on the research of previous members in the Fejer group at Stanford University. In particular, the theory of short-pulse frequency conversion, the QPM technique, and a toolbox of optical circuit components are indispensable to the work in later chapters. We shall first review each of them as the theoretical and technical foundation in the remainder of this chapter.

1.2 Foundations of This Dissertation

1.2.1 Frequency conversion of short optical pulses

This section re-derives the theory of SHG and DFG involving short optical pulses. In the frequency domain, a "short" pulse has a finite bandwidth and cannot be approximated as a delta function. In the time domain, GVM must be considered. Unless otherwise pointed out, group-velocity dispersion (GVD) of the pulses discussed in this dissertation is negligible. This section follows closely the analysis in Ref. [20], where more generalized theory including higher-order dispersion was also presented.

Frequency-domain slowly-varying envelope equation

Assuming plane-wave interactions with a propagation direction z, and a lossless medium, the frequency-domain scalar wave equation can be obtained from Maxwell's equations as [10]

$$\frac{\partial^2}{\partial z^2}\hat{E}(z,\omega) + k^2(\omega)\hat{E}(z,\omega) = -\mu_0\omega^2\hat{P}_{\mathrm{NL}}(z,\omega),\qquad(1.1)$$

where $\hat{E}(z,\omega)$ is the Fourier transform of the electrical field, $\hat{P}_{\mathrm{NL}}(z,\omega)$ is the electric nonlinear polarization at frequency ω, and the wavevector $k(\omega)$ in the medium is related to the refractive index $n(\omega)$ and the speed of light in vacuum, c, by $k(\omega) = \omega n(\omega)/c$. μ_0 is the permeability of free space.

We now restrict this analysis to nonlinear interactions between fields with bandwidths small compared to the optical carrier frequency, and define a frequency-domain

envelope, $\hat{A}(z, \Omega)$, such that $\hat{E}(z, \omega)$ can be written in the form

$$\hat{E}(z, \omega) = \gamma \hat{A}(z, \Omega) e^{-ik(\omega_0 + \Omega)z}, \tag{1.2}$$

where $\Omega = \omega - \omega_0$ is the frequency detuning from a reference carrier frequency ω_0. $\gamma = \sqrt{\frac{2}{nc\epsilon_0}}$, where ϵ_0 is the permittivity of free space. This choice of normalization makes $\left|\hat{A}\right|^2$ equal to the spectral intensity of the corresponding wave. Note that this normalization is different from that in Ref. [20]. Substituting Eq.(1.2) into Eq.(1.1) and assuming a slowly-varying envelope, i.e. $\left|\partial^2 \hat{A}/\partial z^2\right| << \left|k(\omega)(\partial \hat{A}/\partial z)\right|$, we find

$$\frac{\partial}{\partial z}\hat{A}(z, \Omega) = -i\frac{\mu_0 \omega^2}{2\gamma k(\omega)}\hat{P}_{\text{NL}}(z, \omega) e^{ik(\omega_0 + \Omega)z}. \tag{1.3}$$

Physically, we are assuming that $\hat{A}(z, \Omega)$ changes negligibly over the distance of one optical wavelength.

Output SH field and SHG transfer function

Assuming an undepleted pump, the coupled envelope equations that govern the SHG process are

$$\frac{\partial}{\partial z}\hat{A}_1(z, \Omega) = 0 \tag{1.4}$$

$$\frac{\partial}{\partial z}\hat{A}_2(z, \Omega) = -i\frac{\mu_0 \omega_2^2}{2\gamma_2 k_2}\hat{P}_{\text{NL}}(z, \Omega) e^{ik(\omega_2 + \Omega)z}, \tag{1.5}$$

where $\Omega = \omega - \omega_2$ is the detuning from the carrier frequency of the SH pulse, ω_2. Here and in the remainder of this section we use the subscript 1 to denote the FH and the subscript 2 to denote the SH. The nonlinear polarization spectrum, which drives the SH conversion, can be written as

$$\hat{P}_{\text{NL}}(z, \Omega) = \epsilon_0 \gamma_1^2 d(z) \int_{-\infty}^{\infty} \hat{A}_1(z, \Omega')\hat{A}_1(z, \Omega - \Omega') e^{-i[k(\omega_1 + \Omega') + k(\omega_1 + \Omega - \Omega')]z} \, d\Omega', \tag{1.6}$$

where $d(z)$ is the spatial distribution of nonlinear coefficient.

As is well-known from the literature, [20, 21] in undepleted-pump SHG, with or without dispersive broadening, the FH frequency-domain envelope is independent of

z, and the solution to Eq.(1.4) is

$$\hat{A}_1(z, \Omega) = \hat{A}_1(\Omega), \tag{1.7}$$

where $\hat{A}_1(\Omega) \equiv \hat{A}_1(z = 0, \Omega)$. With Eqs. (1.5), (1.6), and (1.7) we obtain the envelope of the SH pulse after an interaction length L as

$$\hat{A}_2(L, \Omega) = \int_{-\infty}^{\infty} \hat{A}_1(\Omega')\hat{A}_1(\Omega - \Omega')\hat{d}[\Delta k(\Omega, \Omega')] \, d\Omega'. \tag{1.8}$$

$\hat{d}(\Delta k)$ is proportional to the spatial Fourier transform of the nonlinear coefficient $d(z)$:

$$\hat{d}(\Delta k) = -i\rho \int_{-\infty}^{\infty} d(z)e^{-i\Delta kz} \, dz, \tag{1.9}$$

where $\rho = \sqrt{\frac{8\pi^2}{n_1^2 n_2 c\epsilon_0 \lambda_1^2}}$. The limits of the integral are extended from [-$L/2$,$L/2$] to $(-\infty, \infty)$ by defining $d(z) \equiv 0$ outside of the interaction length L. The wavevector mismatch is defined as

$$\Delta k(\Omega, \Omega') = k(\omega_2 + \Omega) - k(\omega_1 + \Omega') - k(\omega_1 + \Omega - \Omega'). \tag{1.10}$$

Under the assumptions that GVD and higher-oder dispersion are negligible, Δk becomes independent of Ω', or explicitly $\Delta k = \Delta k_0 + \delta\nu\Omega$, where $\Delta k_0 = k_2 - 2k_1$ is the carrier wavevector mismatch, and $\delta\nu = 1/u_1 - 1/u_2$ is the GVM parameter with the group velocities $u_i = [dk(\omega)/d\omega]^{-1}|_{\omega=\omega_i}$. Hence $\hat{d}[\Delta k(\Omega, \Omega')]$ can be factored out from the integral in Eq.(1.8) and the output SH envelope reduces to a simpler transfer-function result:

$$\hat{A}_2(L, \Omega) = \hat{D}_{\mathrm{SHG}}(\Omega)\widehat{A_1^2}(\Omega), \tag{1.11}$$

where the transfer function:

$$\hat{D}_{\mathrm{SHG}}(\Omega) \equiv \hat{d}(\Delta k_0 + \delta\nu\Omega) = -i\rho \int_{-\infty}^{\infty} d(z)e^{-i(\Delta k_0 + \delta\nu\Omega)z} \, dz, \tag{1.12}$$

and $\widehat{A_1^2}(\Omega)$ is the self-convolution of $\hat{A}_1(\Omega)$:

$$\widehat{A_1^2}(\Omega) = \int_{-\infty}^{\infty} \hat{A}_1(\Omega')\hat{A}_1(\Omega - \Omega')\, d\Omega'. \tag{1.13}$$

The SHG transfer function relates the spectra of the FH and SH. It depends on the dispersive properties of the medium and on the spatial distribution of nonlinear coefficient but not on the input or output pulse parameters. It acts like a passive filter on $\widehat{A_1^2}(\Omega)$. The narrowed spectrum due to filtering is equivalent to a broadened pulse in the time domain. However, this nonlinear filter should be distinguished from a bandpass filter acting directly on the FH spectrum, as $\hat{A}_2(L,\Omega)$ is generated not only from frequency doubling of $\hat{A}_1(\Omega/2)$, but also from sum-frequency generation (SFG) of frequency pairs $\hat{A}_1(\Omega - \Omega')$ and $\hat{A}_1(\Omega')$, for all Ω'. The resulting SH spectral intensity can be higher than that of the FH.

Continuous-wave tuning curve and normalized efficiency

If the input FH field is a monochromatic wave with frequency $\omega_1 + \Omega_1$, the frequency-domain envelope is a delta function:

$$\hat{A}_1(\Omega) = a_1\delta(\Omega = \Omega_1). \tag{1.14}$$

Substituting Eq.(1.14) into Eq.(1.11) we obtain

$$\hat{A}_2(L, \Omega = 2\Omega_1) = a_1^2\hat{D}_{\text{SHG}}(\Omega). \tag{1.15}$$

In a homogeneous medium, $d(z) = d_0\text{rect}(z/L)$, where d_0 is the nonlinear coefficient of the material for the polarizations of the interacting waves, and $\text{rect}(x) = 1$ for $|x| \leq 1/2$ and $\text{rect}(x) = 0$ otherwise. We can calculate the integral in Eq.(1.12), resulting in

$$\hat{A}_2(L, \Omega = 2\Omega_1) = \rho L d_0 a_1^2\text{sinc}\left[\frac{\Delta k(\Omega)L}{2}\right], \tag{1.16}$$

Assuming a cross-sectional overlap area S of the interacting waves, we get the relation

between SH and FH powers:

$$P_2(L, \Omega = 2\Omega_1) = \eta_{\text{nor}} L^2 P_1^2 \text{sinc}^2 \left[\frac{\Delta k(\Omega) L}{2} \right],$$ (1.17)

where the normalized efficiency is

$$\eta_{\text{nor}} = \frac{\rho^2 d_0^2}{S} = \frac{8\pi^2 d_0^2}{n_1^2 n_2 c\epsilon_0 \lambda_1^2 S}.$$ (1.18)

Tuning a constant-amplitude monochromatic wave over the frequency range of interest and recording the SH power is a convenient way to experimentally determine $\left| \hat{D}_{\text{SHG}}(\Omega) \right|^2$, which is also called the continuous-wave (CW) tuning curve.

The above plane-wave interaction results can be modified slightly to treat bulk and guided-wave interactions. In bulk devices, where free space optical beams are focused into the medium, the area S is an overlap of Gaussian profiles. The situation where the beam is focused to a waist at the center of the crystal and the beam size at the crystal edges is $\sqrt{2}$ times the waist is known as confocal focusing, which is close to the optimum condition. In this case $\eta_{\text{nor}} \propto L$. [22]

In guided-wave interactions, mixing takes place between discrete spatial eigenmodes, and a small spot size can be maintained over the entire interaction length, such that $\eta_{\text{nor}} \propto L^2$. Hence waveguide devices use device length much more efficiently than bulk devices. Guide-wave interaction is further discussed in Section 1.2.3.

Output idler field and DFG transfer function

A similar theoretical treatment can be applied to DFG. [23] We consider the process of idler generation from an undepleted pump and an unamplified signal, and use subscript i, s, and p to denote the idler, signal, and pump, respectively. The coupled envelope equations are

$$\frac{\partial}{\partial z} \hat{A}_i(z, \Omega) = -i \frac{\mu_0 \omega_i^2}{2 k_i \gamma_i} \hat{P}_{\text{NL}}(z, \Omega) e^{ik(\omega_i + \Omega)z}$$ (1.19)

$$\frac{\partial}{\partial z} \hat{A}_s(z, \Omega) = 0$$ (1.20)

$$\frac{\partial}{\partial z}\hat{A}_p(z,\Omega) = 0, \tag{1.21}$$

where $\Omega = \omega - \omega_i$ is the detuning from the carrier frequency of the idler pulse, ω_i. The nonlinear polarization is

$$\hat{P}_{\mathrm{NL}}(z,\Omega) = 2\epsilon_0\gamma_s\gamma_p d(z)\int_{-\infty}^{\infty}\hat{A}_s^*(z,-\Omega+\Omega')\hat{A}_p(z,\Omega')e^{-i[k(\omega_s-\Omega+\Omega')+k(\omega_p+\Omega')]z}\,d\Omega'. \tag{1.22}$$

Substituting the freely-propagating solutions of the signal and pump waves, i.e. $\hat{A}_{s,p}(z,\Omega) = \hat{A}_{s,p}(\Omega)$, into Eq.(1.22), we obtain the output idler envelope by integrating Eq.(1.19) (again assuming $d(z) = 0$ outside the interaction length L):

$$\hat{A}_i(L,\Omega) = -i\rho_i\int_{-\infty}^{\infty}d(z)\,dz\int_{-\infty}^{\infty}d\Omega'\,\hat{A}_s^*(\Omega'-\Omega)\hat{A}_p(\Omega')e^{-i\Delta k(\Omega,\Omega')z}, \tag{1.23}$$

where $\rho_i = 2\pi\gamma_s\gamma_p/(\lambda_i n_i)$, and the wavevector mismatch

$$\Delta k(\Omega,\Omega') = k(\omega_p+\Omega') - k(\omega_i+\Omega) - k(\omega_s+\Omega'-\Omega). \tag{1.24}$$

In Ref. [20], the special case of a CW pump was discussed: A transfer-function simplification exists, and Eq.(1.23) describes the spectral inversion of the signal, a function useful for correction of dispersion and nonlinear effects in fiber communication systems. [8] Here we discuss another special case useful in gated OF mixers.

Assume the signal is a CW monochromatic wave at the reference carrier frequency ω_s, i.e. its frequency-domain envelope is a delta function

$$\hat{A}_s = a_s\delta(\Omega = 0), \tag{1.25}$$

We thus have an Ω'-independent Δk and Eq.(1.23) becomes

$$\hat{A}_i(L,\Omega) = \hat{D}_{\mathrm{DFG}}(\Omega)\hat{A}_p(\Omega)a_s, \tag{1.26}$$

where the DFG transfer function

$$\hat{D}_{\mathrm{DFG}}(\Omega) = -i\rho_i\int_{-\infty}^{\infty}d(z)e^{-i\Delta k(\Omega)z}\,dz, \tag{1.27}$$

and

$$\Delta k(\Omega) = k(\omega_p + \Omega) - k(\omega_i + \Omega) - k(\omega_s), \qquad (1.28)$$

where the carrier frequencies are related by $\omega_i = \omega_p - \omega_s$. Under the assumption that $\Omega << \omega_{i,s,p}$ we can perform a Taylor expansion on $\Delta k(\Omega)$. Ignoring GVD and higher-order dispersion, we obtain $\Delta k(\Omega) = \Delta k_0 + \delta\nu_{pi}\Omega$, where $\Delta k_0 = k(\omega_p) - k(\omega_s) - k(\omega_i)$ is the carrier wavevector mismatch and $\delta\nu_{pi}$ is the pump-idler GVM parameter defined by $\delta\nu_{pi} = 1/u_i - 1/u_p$, where u_i and u_p are the group velocities of the idler and the pump pulses, respectively.

$\hat{D}_{\mathrm{DFG}}$ has the form of a linear filter in the frequency domain. Aside from different carrier frequencies, the idler spectrum is a copy of the filtered pump spectrum. We note that the result of Eq.(1.23) still holds if instead of a monochromatic signal, a signal wave with sufficiently narrow spectrum is used. In the time domain it corresponds to a long signal pulse, more precisely $\tau_s >> |\delta\nu_{ps}|L$. Comparing the DFG transfer function with the SHG transfer function of the same frequency-conversion device, we note that for near-degenerate interactions, i.e. $\omega_i \approx \omega_s \approx \omega_1$ (ω_1 is the FH frequency in SHG), they are good approximation of each other.

1.2.2 Quasi-phasematching

In a dispersive medium, the refractive indices at different frequencies are generally different, resulting in non-zero Δk in Eqs. (1.12) and (1.27). With this wavevector mismatch, the interacting waves go out of phase after propagating a distance $L_c = \pi/\Delta k$, or one coherence length. The frequency-mixed output generated over one coherence length converts back to the input wavelengths during the next coherence length. Quasi-phasematching compensates for phase mismatch by changing the sign of the nonlinear coefficient every coherence length. This periodic reversal preserves the direction of energy flow from the input waves to the output waves, ensuring that the output increases monotonically with propagation distance. [16] (Figure 1.6)

The periodic variation of the nonlinear coefficient produced by a QPM grating
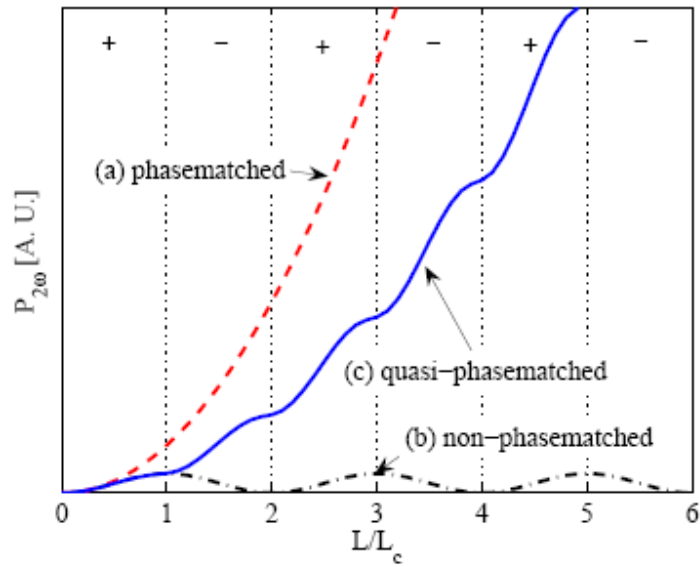
Figure 1.6: SH power in the propagation direction under (a) perfectly phasematched, (b) non-phasematched, and (c) quasi-phasematched conditions. Quasi-phasematching ensures monotonic growth of SH power albeit with a reduced efficiency compared to perfect phasematching.

with period Λ_g can be represented by the following Fourier series:

$$d(z) = d_0 \sum_{m=-\infty}^{\infty} G_m e^{imk_g z} \qquad (1.29)$$

where $k_g = 2\pi/\Lambda_g$, and for a uniform grating the Fourier coefficients are $G_m = \frac{2}{m\pi}\sin(m\pi D)$, where D is duty cycle. A first-order QPM grating with 50% duty cycle and length L is represented by

$$d(z) = \frac{2}{\pi}d_0 e^{ik_g z}\mathrm{rect}\left(\frac{z}{L}\right). \qquad (1.30)$$

We define $d_{\mathrm{QPM}} \equiv 2d_0/\pi$ for the rest of this dissertation. Substituting Eq.(1.30) into Eq.(1.12), we find that compared with a homogeneous medium, a first-order QPM grating has an effective nonlinear coefficient d_{QPM} and shifts the wavevector mismatch to $\Delta k' = \Delta k - k_g$. If k_g is chosen to phasematch the carrier frequencies, then $\Delta k' = \delta\nu\Omega$, where $\delta\nu$ is the previously defined GVM parameter. Eqs. (1.16) through (1.18) take the same functional form with the re-defined nonlinear coefficient d_{QPM} and wavevector mismatch $\Delta k'$.
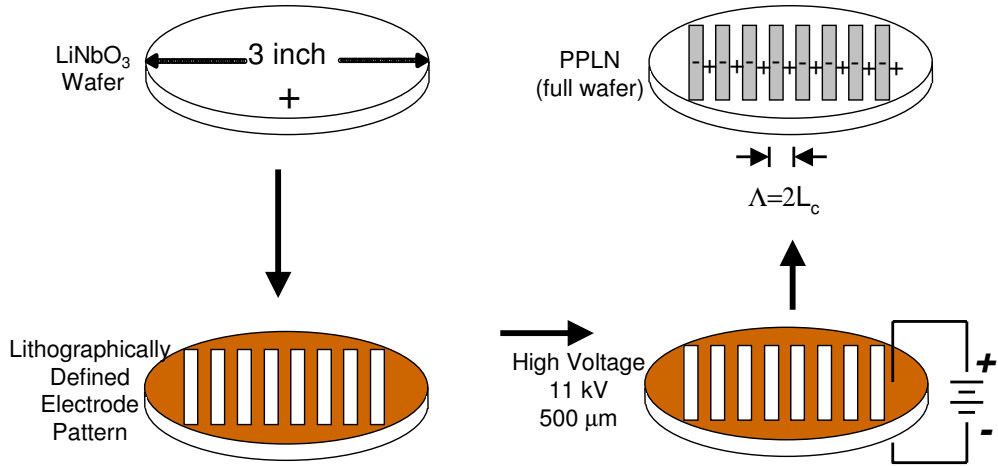
Figure 1.7: Whole-wafer electric-field poling of lithium niobate.

QPM structures are most commonly obtained by periodic poling of ferroelectric

crystals like LiNbO$_3$, LiTaO$_3$, and KTP. The standard electric-field-poling technique for congruent lithium niobate is described in Refs. [22, 24] and the procedures are shown in Figure 1.7. The principle is that the spontaneous polarization in a ferroelectric material can be reversed under a sufficiently large electric field. Since the sign of the nonlinear susceptibility changes with the orientation of the ferroelectric domains, patterning a periodic array of domains creates a periodic grating in the sign of the nonlinear susceptibility. All QPM devices in this dissertation were fabricated using this method. A detailed theoretical treatment of QPM can be found in Ref. [16].

1.2.3   Guided-wave interactions and a toolbox of optical circuit components

Integrated optical circuits compatible with PPLN have further extended the functionality of optical signal processors. They are based on guided-wave interactions and the basic building blocks include reverse-proton-exchange (RPE) waveguides, small-radius bends, wavelength-selective directional couplers, and Y-junctions. We review their basics below.

Guided-wave interactions

For simplicity, we assume that only a single waveguide mode participates in the interaction at each wavelength. Thus Eq.(1.2) is modified to

$$\hat{E}(x, y, z, \omega) = \gamma \hat{A}(z, \Omega) e(x, y) e^{-ik(\omega_0 + \Omega)z}, \tag{1.31}$$

where $e(x, y)$ is the normalized transverse field profile and is defined by

$$\int_{-\infty}^{\infty} \int_{-\infty}^{\infty} e^2(x, y) \, dx \, dy = 1. \tag{1.32}$$

The above normalization makes $\left|\hat{A}\right|^2$ equal to the power spectral density of the corresponding mode.

For guided-wave nonlinear interactions, the local amplitude of the nonlinear coupling depends on an overlap integral of the interacting waveguide modes with the

spatially varying nonlinear coefficient, $d(x, y, z)$. If $d(x, y, z)$ is periodic in z, as would be the case for a simple QPM interaction, it can be written as

$$d(x, y, z) = d_0 \sum_{m=-\infty}^{\infty} G_m(x, y) e^{imk_g z}, \tag{1.33}$$

where the Fourier coefficient $G_m(x, y)$ is given by

$$G_m(x, y) = \frac{1}{d_0 \Lambda_g} \int_{-\Lambda_g/2}^{\Lambda_g/2} d(x, y, z) e^{-imk_g z} \, dz. \tag{1.34}$$

In this case the overlap integral is given by [25, 26]

$$\vartheta_m = \int_{-\infty}^{\infty} \int_{-\infty}^{\infty} G_m(x, y) e_1^2(x, y) e_2^*(x, y) \, dx \, dy. \tag{1.35}$$

$e_1(x, y)$ and $e_2(x, y)$ are normalized eigenmodes of the waveguide at the FH and SH wavelengths, both calculable using the model in Ref. [27] and measurable in experiments.

If $d(x, y, z)$ has an additional variation with respect to z that is slow enough that a local Fourier coefficient $G_m(x, y, z)$ can reasonably be defined, we can calculate a local overlap integral $\vartheta_m(z)$ by replacing $G_m(x, y)$ in Eq.(1.35) with $G_m(x, y, z)$. In a PPLN device, the periodicity comes from the QPM grating with period Λ_g, while the slowly-varying component can be a result of duty-cycle modulation or transverse patterning of the grating. The application of the latter is discussed in Chapter 3.

For the purposes of this dissertation, we assume that the power of the FH wave can vary along the propagation direction z with a known function $P_1(z)$, with the variation controlled, for example, with a directional coupler. We can then define a local nonlinear coupling strength $\kappa_m(z)$, where

$$\kappa_m(z) = \vartheta_m(z) P_1(z). \tag{1.36}$$

With this definition, the SH output power for an interaction with mth-order quasi-phasematching, P_{2m}, in the low conversion and lossless limit, is given by

$$P_{2m} = \frac{8\pi^2 d_0^2}{n_1^2 n_2 c\epsilon_0 \lambda_1^2} \left| \int_0^L \kappa_m(z) e^{-i\Delta k_m' z} \, dz \right|^2 , \tag{1.37}$$

where $\Delta k_m' = k_2 - 2k_1 - mk_g$.

RPE waveguides, mode filters, and tapers

The RPE process has been an important technique for fabricating low-loss optical waveguides in LiNbO$_3$. RPE buries annealed-proton-exchange (APE) waveguides [28] beneath the surface of the substrate and improves the mode overlap of the interacting waves. [2] An empirical model has recently been developed to accurately calculate the refractive-index profile in RPE waveguides based on the waveguide width (mask opening), proton-exchange depth, and the annealing and reverse-proton-exchange times. [27] The fabrication procedures for RPE waveguides are illustrated in Figure 1.8. The conventional RPE recipe is 1.84-μm initial proton-exchange depth, 23-hr annealing at 310 °C, 26-hr reverse-proton-exchange at 300.5 °C.
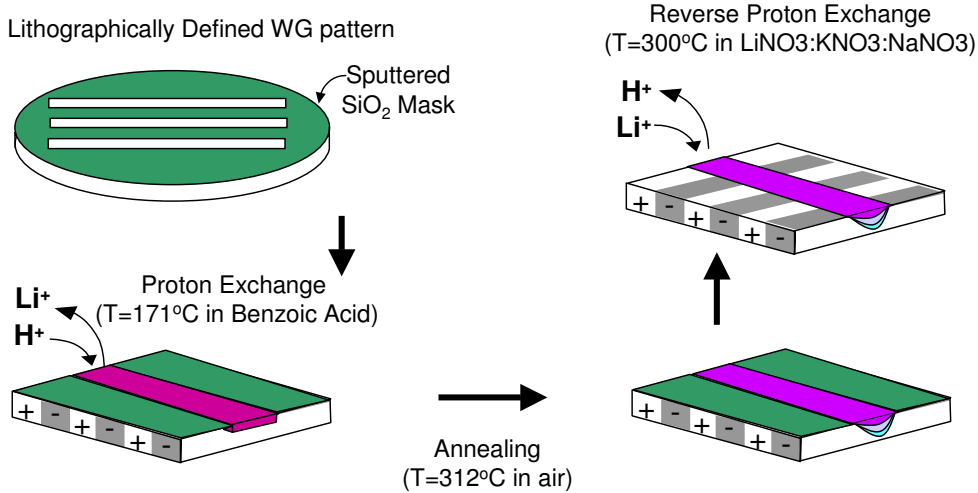
Figure 1.8: Fabrication of RPE waveguides.

A typical RPE waveguide (shown in Figure 1.9) starts with a 3.5-μm-wide mode-filter, which supports only the TM$_{00}$ mode. The wave remains TM$_{00}$ through an
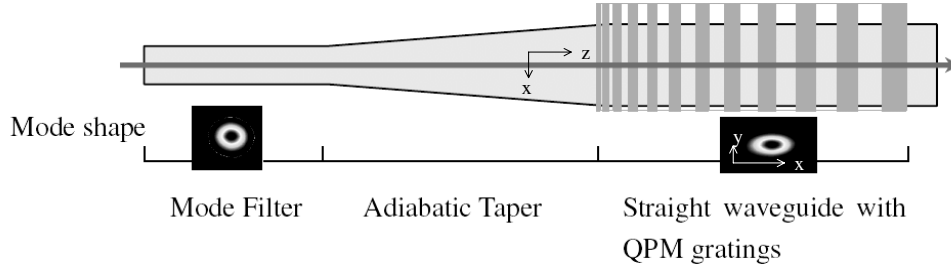
Figure 1.9: Schematic of a straight waveguide with mode filter and taper (mode pictures rotated by 90 °).

adiabatic taper into the straight section with a 7.5-μm width, which supports several transverse modes at 1.5-μm wavelength and is the width which is noncritical for phasematching SHG around 1.5 μm. The noncritical phasematching width is the one for which the FH-SH wavevector mismatch does not have first-order dependence on the waveguide width, and hence the tolerance on fabrication error is the largest. [25] When efficient use of the length of the wafer is of concern, the taper width is designed to grow quadratically in the propagation direction, reducing the necessary length of the taper while preserving its adiabatic property.

With the tight confinement of the interacting waves, good mode overlap, η_{nor} is approximately $100\%/\mathrm{W/cm^2}$ in a typical RPE PPLN waveguide. [2]

Deep exchange waveguides and small radius bends

Tight bends with small radii are desired in optical circuits for denser integration. The limiting factor is the increasing radiation loss with smaller bend radii. For conventional RPE waveguides the smallest cosine-bend radius with negligible bending loss is 4 mm. With a larger initial exchange depth of 2.39 μm, the smallest radius for cosine bends with negligible bending loss reduces to 1 mm. The smaller bending loss results from an increased effective refractive index and reduced mode size in the dimension of the waveguide width. Correspondingly the noncritical waveguide width becomes 6.5 μm.

The 2.39-μm proton-exchange depth is optimized for a balance between the smaller bend loss and the higher propagation loss associated with a higher proton dose. The

propagation loss is <0.4 dB/cm, compared to <0.1 dB/cm for conventional RPE waveguides.

A circular bend has a constant curvature over the entire length and is much lossier than a cosine bend with the same minimum bend radius. We experimentally determined the circular-bend radius with negligible bending loss to be 2 mm with the deep exchange recipe. U-turns with such a small bend radius are used in applications such as the single-chip OTDM-MUX in Chapter 4.

Wavelength-selective directional couplers

Many integrated optical circuits require the transfer of optical power from one waveguide to another. According to basic coupled-mode theory, this transfer can be accomplished by placing two parallel waveguides close enough so that their modes begin to overlap. If the two waveguides are identical, optical power transfers from one waveguide to the other according to

$$P(z) = P_0 \sin^2\left(\frac{\pi L}{2L_{\mathrm{dc}}}\right) \tag{1.38}$$

Here L_{dc} is the coupling length for complete power transfer, which can be estimated by $L_{\mathrm{dc}} = (\lambda/2)/(n_1 - n_2)$, where n_1 and n_2 are the effective refractive indices for the two lowest-order eigenmodes of the combined structure. [29] Wavelength-selective filters and combiners can be implemented by taking advantage of the different coupling length for different wavelengths. Although we can use the waveguide model to obtain the eigenmodes for a directional coupler and estimate the coupling length, >20% error may exist in such estimation. In practice we empirically determine the length of a directional coupler for a chosen spacing between the two waveguides. For a typical design using the noncritical waveguide width, 3-μm separation and 1550-nm wavelength, L_{dc} is 3 mm with conventional RPE and 1.8 mm with deep RPE. For both these designs, the coupling at the SH wavelength is below 1%.

In practice, for the noncritical phasematching waveguide widths, L_{dc} is sensitive to perturbations in waveguide separation caused by the photolithographic process. A "non-critical" coupler has been developed using narrower RPE waveguides. [30]

Mode multiplexers and demultiplexers

While not directly used in this dissertation, multiplexing higher-order waveguide modes provides a new solution to the problem of distinguishing and spatially separating the interacting waves in OF mixers. [31, 32] Asymmetric Y-junctions that are compatible with standard PPLN devices have been demonstrated as mode multiplexers and demultiplexers with a contrast exceeding 30 dB. [33]
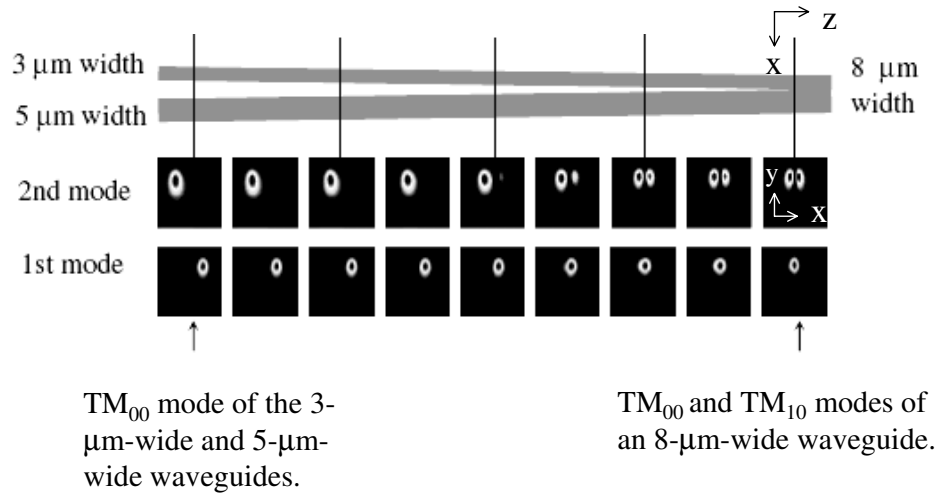
Figure 1.10: Mode evolution in an adiabatic asymmetric Y-junction (mode pictures rotated by 90 °).

In an adiabatic asymmetric Y-junction, the lowest-order modes of the wide and narrow port evolves into the first and second modes of the combined structure, respectively. Launching into the narrow "odd port" of an asymmetric Y-junction converts a TM_{00} mode into a TM_{10} mode, while launching into the wider "even port" leaves the mode unchanged. (Figure 1.10) Viewed in the opposite propagation direction, the junction acts as a TM_{00}-mode/TM_{10}-mode demultiplexer. Shape optimization in transverse and longitudinal directions has been studied to shorten the length of the Y-junction while preserving mode contrast. [34]

Chapter 2

Quasi-group-velocity Matching

2.1   Introduction

Optical frequency mixers based on PPLN waveguides are among the highest speed optical signal-processing devices available today. They have been used to demonstrate many important all-optical signal-processing functions. With a CW local oscillator, a standard C-band OF mixer has over 1 THz of conversion bandwidth. However, to fully exploit the capacities of OF mixers as all-optical digital signal-processing elements, [4] a gated mixer where the local oscillator consists of short optical pulses is often used. Because pulses at different wavelengths propagate at different velocities, the speed limit of a gated mixer is set by the group-velocity mismatch between the interacting waves. [35] In SHG, as we have seen in Section 1.2.1, the SH spectrum is limited by the finite transfer-function bandwidth of the mixer, and GVM results in limited peak amplitude and longer pulse duration. In optical parametric generation (OPG), GVM adversely affects the temporal properties of the output. [36] In optical communications, at high enough bit rate, crosstalk can occur when the pump pulse walks off the data into a neighboring time slot, as shown in Figure 2.1.

Given the required bandwidth of a device, GVM limits the maximum interaction length for short pulses. On the other hand, the conversion efficiency is proportional to the square of the interaction length in SHG and to the fourth power of that length in cascaded processes. [6] For 3-ps pulses, typical of 160-Gbit/s systems, the maximum
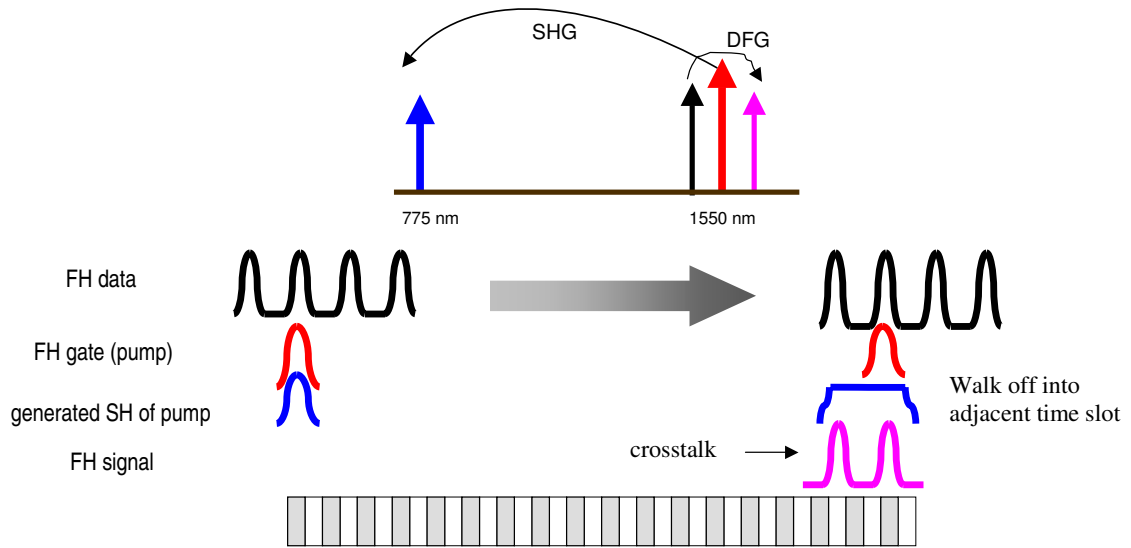
Figure 2.1: An example of GVM causing crosstalk in a gated mixer through cascaded SHG/DFG. The SH of the gate broadens and mixes with the data pulse in the next time slot.

interaction length is about 8 mm in a PPLN OF mixer, only 1/6 that of a standard device. It is thus very useful to have some group-velocity matched structure so that the interaction length is no longer limited to one walk-off length, thereby obviating the bandwidth/efficiency trade-off.

Group-velocity-matched SHG has been demonstrated in a variety of birefringent phasematching and quasi-phasematching materials, but only at specific frequencies determined by the dispersion of the nonlinear material. [37, 38, 39] For example, in lithium niobate, the FH and SH group velocities are matched in a type 0 ($e + e \rightarrow e$) interaction only at a FH wavelength near 2.6 μm. [40] For PPLN devices, a technique that makes use of spectral angular dispersion can provide GVM compensation for arbitrary frequencies, but the non-collinear geometry limits its use to bulk devices. [41]

The work in this chapter addresses the bandwidth/efficiency trade-off of waveguide-based OF mixers. We demonstrate how integrated-optic structures can mitigate this trade-off and extend the functionality of optical signal-processing devices. With a

toolbox of optical circuit components, we are able to develop a broadband mono-lithic quasi-group-velocity-matching (QGVM) scheme. The remainder of this chapter is devoted to the design and demonstration of the QGVM scheme. Section 2.2 describes the theory and groundwork for device design, including the measurement of the important GVM parameter. In Section 2.3 I present the experimental demonstration of a prototype device. This device can be iterated to further increase the bandwidth/efficiency product until a length is reached where group-velocity dispersion becomes significant. This and other practical limitations are discussed in Section 2.4.

2.2   Theory and Groundwork

GVM is quantified by a single parameter $\delta\nu = 1/u_1 - 1/u_2$, defined as the difference in reciprocal group velocities of the interacting waves. In SHG, the characteristic length over which the FH and SH pulses walk off each other is called the group-velocity walk-off length, i.e. $L_{gv} = \tau_1/|\delta\nu|$, where τ_1 is the FH pulse width; for interaction length $L > L_{gv}$, the generated SH pulse is limited in peak amplitude, and its duration becomes $\tau_2 = |\delta\nu|\,L$. If an FH and an SH pulse propagate a length L, the time delay of one pulse with respect to the other is $\Delta t = |\delta\nu|\,L$. A frequency-domain description of the process is detailed in the short-pulse SHG theory in Section 1.2.1.

A precise measurement of $\delta\nu$ in waveguides is critical to the design of QGVM devices. The SHG tuning curve of devices with segmented QPM gratings provides a convenient measure of $\delta\nu$. Segmentation with millimeter-scale periodicity Λ_s adds low spatial-frequency components to the grating vector k_g, and modulates the wavelength tuning curve on a nanometer scale. With such a segmented grating, the total wavevector mismatch becomes $\Delta k = k_2 - 2k_1 - k_g - 2n\pi/\Lambda_s$, where n is an integer. It is easy to see that the tuning curve has peaks at $\delta\nu\Omega = 2n\pi/\Lambda_s$. Here Ω is the detuning from the carrier QPM frequency ω_2. A measurement of the periodicity of the peaks of the tuning curve determines $\delta\nu$. This method is less sensitive to imperfections in the waveguide or grating than is a measurement of the width of the single peak of a uniform grating, and hence is a more accurate method to determine $\delta\nu$.
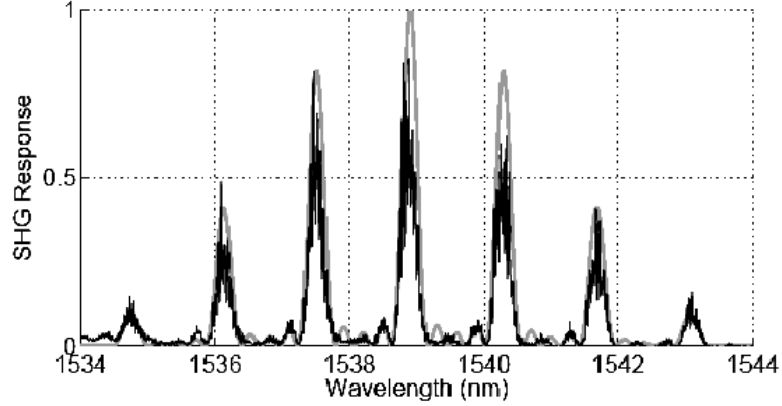
Figure 2.2: Measured (black) and calculated (grey) tuning curves of a segmented QPM grating; the best fit to the periodicity yields a precise value of $\delta\nu = 0.36$ ps/mm.

Figure 2.2 shows the SHG response for an APE waveguide device with $\Lambda_s = 8$ mm (2-mm QPM segments separated by 6 mm). From the 1.39-nm modulation period we infer that $\delta\nu = 0.36$ ps/mm around 1540 nm. As expected, this number is slightly larger than the 0.30 ps/mm bulk value.

With an accurate value for $\delta\nu$, the design of a QGVM device is straightforward. The schematic and geometry of a QGVM device is shown in Figure 2.3. After a first QPM grating, the FH pulse is selectively coupled into a parallel waveguide by a directional coupler, delayed by a small-radius bend, and then coupled back into the original waveguide, now synchronized to the SH pulse. Therefore the SH pulse generated in the second QPM grating overlaps with the first one. A single QGVM stage doubles the effective interaction length for the pulses, and hence quadruples the SHG efficiency without sacrificing bandwidth.

We denote the path length of the FH pulse as L_1 and that of the SH pulse as L_2. L_1 and L_2 both include the common path of one QPM grating and two directional couplers. L_1 is slightly longer than L_2 due to bending. In front of the second QPM grating, the two pulses should be synchronized

$$L_1/u_1 = L_2/u_2, \tag{2.1}$$
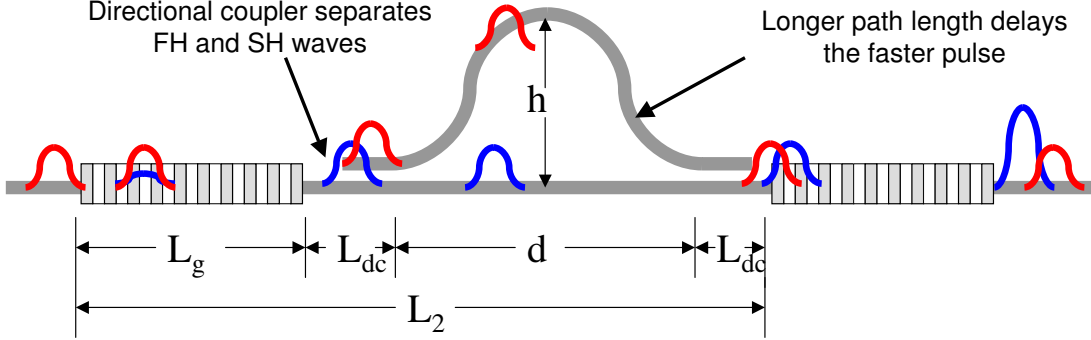
Figure 2.3: The schematic and geometry of a QGVM device using integrated wave-guide structures. L_{bend} is the length of the bend over span d; L_1 differs from L_2 only by replacing d with L_{bend}. L_1 and L_{bend} are not shown on the figure.

or equivalently

$$(L_1 - L_2)/u_1 = \delta\nu L_2. \tag{2.2}$$

L_1 and L_2 are related to the geometry of the QGVM device by

$$L_1 = L_{bend} + 2L_{dc} + L_g \tag{2.3}$$

$$L_2 = d + 2L_{dc} + L_g \tag{2.4}$$

$$L_{bend} = \frac{2d}{\pi} E\left[-\left(\frac{\pi h}{d}\right)^2\right] \tag{2.5}$$

$$r_{min} = \frac{d^2}{2\pi^2 h}, \tag{2.6}$$

where L_{dc}, L_g, and L_{bend} are the lengths of the directional couplers, QPM gratings, and cosine bend, respectively, d, h, and r_{min} are the span, height, and minimum radius of the bend, and function $E(x)$ is the complete elliptic integral of the second kind. [42] When designing a QGVM device, given r_{min}, one numerically solves Eqs. (2.2) through (2.6) to obtain d and h.

Correct choice of d and h ensures that the SH pulses generated in the two QPM gratings overlap in time. However, because of the difference between group-velocity

and phase-velocity, the overlap of envelopes does not automatically ensure that the carrier phase under the envelopes are the same. Only when the SH pulses generated in the two sections are in phase, will they interfere constructively so that energy flows from FH to SH in the second QPM grating. Successful operation of the device requires the carrier phase of the pulses be correct in addition to synchronizing the envelopes. Meeting this condition requires precise positioning of the QPM gratings. Given the difficulty in calculating the absolute phase shift through the directional couplers and bends, we designed the device to use temperature tuning to meet this requirement. The relative phase of the pulses changes with temperature, as a result of the change in effective refractive index and the thermal expansion of the crystal. When ΔT is small, we have

$$\phi\left(\Delta T\right) = \frac{2\pi}{\lambda_2}\left(\frac{dn_2}{dT}L_2 - \frac{dn_1}{dT}L_1\right)\Delta T + \frac{2\pi}{\lambda_2}\left(n_2 L_2 - n_1 L_1\right)\zeta_{LN}\Delta T, \qquad (2.7)$$

where ϕ is the relative phase of the two SH pulses, ΔT is temperature change, λ_2 is the SH wavelength in vacuum, n_1 and n_2 are the effective refractive indices at the FH and SH wavelengths, and ζ_{LN} is the thermal expansion coefficient of lithium niobate. The first term on the right-hand side of the equation is the phase change due to the changed refractive indices and the second term is the phase change due to thermal expansion. We have omitted the ΔT^2 terms. As an example, given $L_1 = 15.8$ mm, $L_2 = 15.0$ mm, $\zeta_{LN} = 1.54 \times 10^{-5}$ K^{-1}, $n_1 = 2.149$, $n_2 = 2.201$, $dn_1/dT \approx dn_2/dT = 1.1 \times 10^{-4}$ K^{-1}, and $\lambda_2 = 775$ nm, one needs a temperature change of approximately 8 °C to tune the phase by 2π. Therefore given any initial phase of the two SH pulses, a temperature tuning of ± 4 °C is enough to obtain optimum operation.

2.3 Experimental Demonstration

To demonstrate this QGVM scheme, we fabricated our devices on a z-cut LiNbO$_3$ chip. The waveguides were proton-exchanged to an initial depth of 0.7 μm and annealed for 26 hours at 325 °C. The waveguides begin with 4-μm-wide mode filters and widen gradually through a taper to the 8-μm noncritical QPM width. [25] The

bends, also 8-μm wide, have a radius of 4 mm, the smallest radius for which the additional loss due to bending is negligible for this type of waveguide. The lengths of the bends range from 10.18 to 13.61 mm, exceeding the lengths of the straight waveguides by 0.36 to 0.80 mm, providing a different time delay in each device. The directional coupler at each end of the bend is 1.7-mm long and consists of two 8-μm-wide parallel waveguides separated by 3 μm. It is designed to couple out more than 99% of the FH but have negligible coupling at the SH (typically below 1%). Two sections of QPM gratings are adjacent to the directional couplers. They are 0.269-mm and 0.538-mm long, respectively, with a QPM period of 15 μm. This choice of grating lengths differs from the nominal design, but allows for convenient testing by generating two clearly distinguishable pulses. A reference device without the bend but otherwise identical to the full devices was fabricated adjacent to each set for comparison purpose. The GVM parameter we used in designing all devices was 0.36 ps/mm, obtained in experiments described in Section 2.2.

When testing the devices, we used 150-fs pulses with a center FH wavelength of 1545 nm generated by an optical parametric oscillator (Spectra-Physics OPAL) at an 82-MHz repetition rate. The OPAL was pumped by a mode-locked Ti:sapphire laser (Spectra-Physics Tsunami). The FH pulse was split into pump and reference beams. The pump beam, attenuated to an average power of 0.5 mw, was coupled into the PPLN device to generate the SH signals. The reference beam passed through a delay line and then cross-correlated with the SH signals through two-photon absorption in a GaAsP photodiode. [43] The device was heated to 75 °C to suppress photorefractive effects. [44]

Figure 2.4 shows the time-resolved signal power of a reference device together with four QGVM devices. Reference device (a) has no GVM compensation, and two SH pulses are generated 6 ps apart. The energy in the first pulse is roughly four times that of the second one, as expected for our design with one grating being 0.7 walk-off-lengths long, and the other one twice as long. The pulse widths are measured to be 150 fs and 180 fs after deconvolution of the 150-fs reference pulse, consistent with calculations [10] using the grating lengths and FH pulse width. The first pulse becomes slightly longer than the second one because it propagates a longer distance

and hence undergoes more GVD at the SH wavelength. In devices (b) through (d), GVM is partially compensated, and the two pulses move closer as the added delay increases toward 6 ps. Finally in device (e), the two pulses are very well synchronized as we expect. The offset of the two envelopes after compensation is measured to be less than 80 fs.
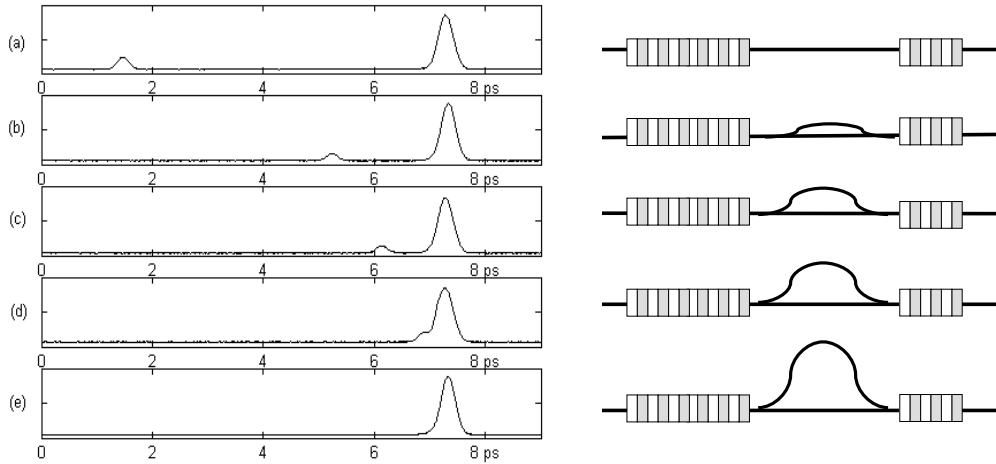
Figure 2.4: The measured cross-correlation traces of two SH pulses generated in two QPM gratings. The pulses move closer together as the amount of GVM compensation increases. In device (e) the envelopes of the two pulses are synchronized to within 80 fs.

Figure 2.5 shows the temperature-tuning results of the device in Figure 2.4(e). In an 8-°C cycle, the two overlapping pulses go between in-phase and out-of-phase, and hence the output optical power assumes maximum and minimum values alternately. This temperature tuning is small enough compared to the approximately 250-°C temperature-tuning bandwidth of the short QPM gratings we used, so that it does not shift the phasematching wavelength of the gratings. Furthermore, over the 8-°C range, the overlap of the pulse envelopes is not affected. This is critical to the successful operation of the device: the necessary temperature change to obtain the correct phase is not so large as to move the envelope of one pulse off the other, nor is it so small as to impose a strict temperature stability requirement for a stable output.
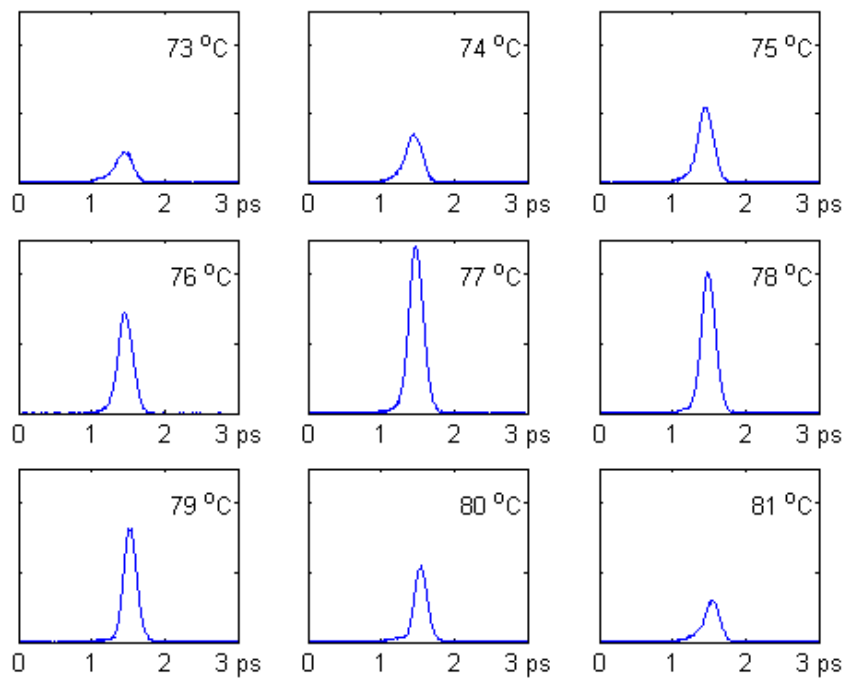
Figure 2.5: Temperature tuning was used to achieve the optimal operation condition for the device. The carrier phase of the two pulses were tuned by 2π in an 8-°C cycle. The two SH pulses went alternately between destructive and constructive interference.

2.4   Further Discussion

As shown in Figure 2.6, the QGVM structure can be iterated to further increase the
bandwidth/efficiency product, which in SHG grows quadratically with the number
of QPM sections. There are, however, fundamental limitations imposed by GVD on
multi-stage QGVM (MQGVM) devices.
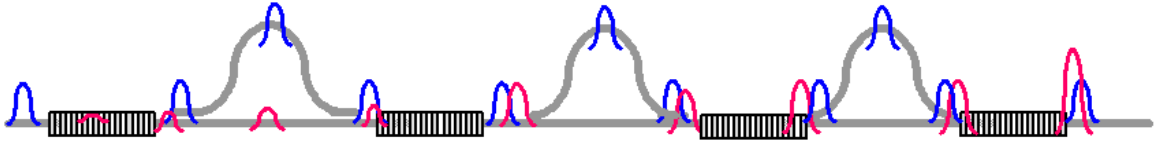
Figure 2.6: The schematic of a MQGVM device: four interaction sections will increase
the bandwidth/efficiency product by a factor of 16 for SHG.

Although GVM is compensated for after each QGVM section, an initially transform-
limited Gaussian pulse of duration τ_0 propagating a distance l in a medium with GVD
parameter β_2 is nevertheless broadened to $\tau_2 = \tau_0\sqrt{1 + (l\beta_2/\tau_0^2)^2}$. [45] τ_2 is a strong
function of the initial pulse duration, τ_0, and is also determined by wavelength (hence
β_2) and propagation distance l. Beyond the point that pulse broadening due to GVD
is negligible, the bandwidth of the device is limited by GVD, and further GVM com-
pensation no longer helps. We shall now estimate the maximum bandwidth/efficiency
enhancement one can achieve by iterating the QGVM structure.

Considering SHG of 1550-nm pulses in PPLN, the dominating GVD is at the SH
wavelength where $\beta_2 = 460$ fs^2/mm. [40] The total propagation distance l is related
to the number of QPM sections n by $l = (n-1)L_2 + L_g$. It is further related to bend
radius r_{min} with Eqs (2.3) through (2.6). Assuming that the largest tolerable pulse
broadening is 50%, which is an arbitrary choice but does not affect the generality of the
analysis, we plot the relation between the number of QPM sections and required bend
radius in Figure 2.7 for 100-fs and 150-fs pulses. The tightest bend we can make with
our current RPE waveguide technology is 1 mm, which allows bandwidth/efficiency
enhancement of 16 and 64 times for 100-fs and 150-fs pulses, respectively, before the
GVD effect becomes significant.

Besides GVD, there are other practical limitations on MQGVM devices. If the
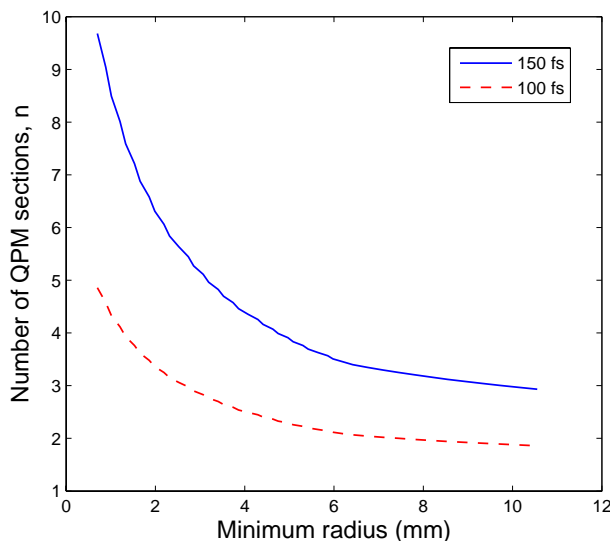
Figure 2.7: The effect of GVD on MQGVM devices. The more QPM sections, and the shorter the original pulse duration, the smaller the bend radius required to stay away from significant pulse broadening due to GVD.

total device length is too long, given the linear space of a 3-inch wafer, it can be challenging to integrate all compensation stages on a single chip. One solution is to fabricate a U-turn bend to use twice the chip length, as is demonstrated for another application in Chapter 4. However, with a longer device and the deep exchange waveguide, the propagation loss could become significant.

In theory, because of fabrication variations, a single temperature does not automatically ensure correct phase relations among all MQGVM stages. However, since the relevant phase relation is the same as the one that governs phasematching in a QPM grating, the precision requirement is on the order of a half grating period. Just as the fabrication precision has enabled >50-mm-long QPM gratings, consistent phase over that length for MQGVM devices should not come up as an issue. This was confirmed by experiments in which MQGVM was used to achieve near transform-limited OPG output. [36]

Chapter 3

Amplitude Modulation of QPM Interactions

3.1 Introduction

While uniform QPM gratings have enabled many important all-optical signal-processing functions, since the early days of QPM devices various techniques to engineer QPM gratings have been developed to expand their functionality. Grating periods are chirped to cover the wide bandwidth of femtosecond pulses and provide pulse compression and shaping; [10, 46] transverse patterning is used in bulk to study nonlinear physical optics [47] and together with angled gratings for odd-even mode mixers in waveguide devices; [48] multi-channel devices that require simultaneous phase-matching of several wavelengths in one grating are made possible by grating phase modulation and aperiodic structures. [7, 49, 50, 51]

With all of the above developments, until recently a convenient technique to modulate the amplitude of QPM interactions has not been available. Amplitude modulation is difficult for a device based on ferroelectric domain reversal, because unlike electronic filters to which virtually any analog window function can be applied, [52] a QPM grating is a digitized structure with a local nonlinear coefficient being either plus or minus that of the material. Nevertheless, modulating the amplitude of QPM interactions is important, because the frequency response (tuning curve) of a

nonlinear device is proportional to the Fourier transform of the spatial distribution of nonlinear coupling (Eq.(1.37)), and the ability to shape the output spectrum will open up many new possibilities for optical signal processing.

For example, the tuning-curve shape of a frequency conversion device is important in optical communications, where crosstalk between data channels is to be avoided. Ideally, in a nonlinear mixing process, only the channel whose wavelength corresponds to the center peak of the tuning curve should undergo frequency conversion. However, as a result of the existence of tuning curve sidelobes, those channels whose wavelengths correspond to the side peaks will also be converted, and thus introduce crosstalk in many applications. [53, 54]

The intrinsic sinc-square tuning curve of a uniform grating is unsatisfactory in that the ratio between its first side peak and main peak is only -13 dB, and its sidelobes decay only quadratically with detuning, whereas in-band crosstalk below -30 dB is often required for communication systems. [55, 56] To meet this goal, a sidelobe-free tuning curve is most desirable.

Fourier-transform analysis shows that the tuning curve sidelobes can be suppressed if the QPM interaction is apodized, i.e. the hard edges removed and the nonlinear coupling brought to zero smoothly along the length of the device. [57] Some commonly used apodization functions and their transfer functions have been compiled in Ref. [58]. While apodization suppresses sidelobes, it also results in reduced peak efficiency and broadening of the main peak. These factors must be balanced when selecting an appropriate apodization function.

In this chapter, I present several techniques to effectively modulate the local amplitude of QPM interactions in PPLN waveguides, and the experimental demonstration of sidelobe-suppressed tuning curves using each of these techniques.

3.2   Different Approaches

It is in principle possible to modulate the effective nonlinear coefficient, d_{eff}, by locally changing the duty-cycle, D, since for first-order QPM, $d_{\text{eff}} = d_{\text{QPM}} \sin(\pi D)$. In

practice, however, an adequate modulation with d_{eff} being 10% that of a 50%-duty-cycle grating would require $D \approx 3\%$. This small duty cycle corresponds to a domain length of 0.5 μm for a C-band PPLN device, currently not easily controlled given the domain growth mechanism of congruent lithium niobate undergoing periodic poling. [24] For QPM devices in other materials, or for frequency conversion of longer wavelengths (hence longer domain length), duty-cycle control could be a practical option for amplitude modulation.

The nature of guided-wave interaction (presented in Eqs. (1.33) through (1.37)) makes possible a number of techniques to modulate the local amplitude of nonlinear coupling that do not necessarily involve modulating d_{eff} itself.

Mode-overlap control

$G_m(x, y, z)$ in Section 1.2.3 can be defined in lithography by carefully positioning the QPM gratings. With the gratings patterned into and out of the waveguide, the overlap of the waveguide mode with the nonlinearity of the periodically poled material is modulated. (Figure 3.1) This mode-overlap-control approach, although different in realization and application, bears similarity to the previously demonstrated odd-even mode QPM by angled and staggered gratings, [48] in that they both manipulate the overlap integral by changing $G_m(x, y, z)$. With this mode-overlap control, the overlap integral can vary continuously from zero to a maximum, and virtually any spatial profile of $\vartheta_m(z)$ can be obtained by a lithographically defined poling pattern.
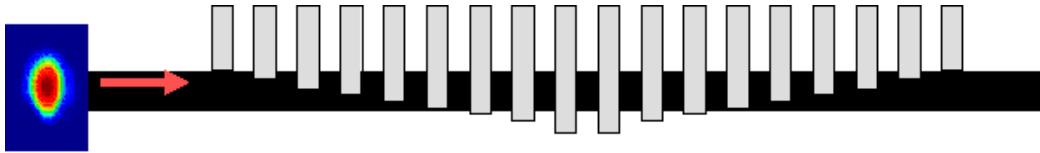
Figure 3.1: The schematic of a mode-overlap-control device. The overlap of waveguide mode with grating reversals is changed along the propagation direction to modulate the spatial dependence of the nonlinear coupling.

Double couplers

An alternative to the above scheme, which modulates $\vartheta_m(z)$, is to instead modulate $P_1(z)$ in Eq.(1.36). This modulation can be realized by integrating two wavelength-selective directional couplers with a QPM grating, as shown in Figure 3.2. The FH

power is coupled into and out of the QPM grating by the two couplers. With a constant-gap constant-waveguide-width coupler, $P_1(z)$ and hence $\kappa_m(z)$ of the QPM grating in either coupler region vary with a cosine-square function, although the grating itself is uniform.
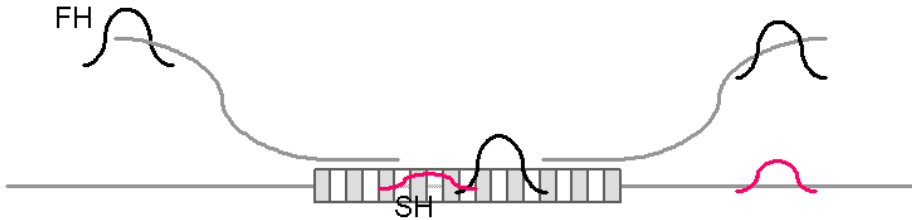
Figure 3.2: The double-coupler structure modulates the FH power and hence the nonlinear coupling in a waveguide, although the grating itself is uniform.

Deleted reversals
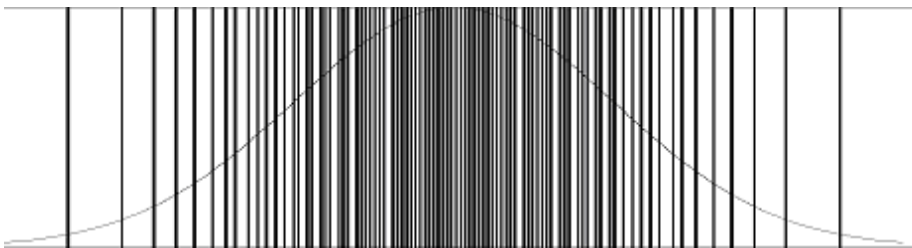
Figure 3.3: The deleted-reversal grating and the target function of $\kappa_1(z)$.

A third scheme uses a deleted-reversal pattern to directly modulate the amplitude of the QPM grating, and match the spatial profile of nonlinearity to a target function. (Figure 3.3) The reversals are deleted in such a way that the nonlinear coefficient integrated over any two endpoints of the grating equals that of the target function. In the algorithm, two endpoints start from the center of a uniform grating and move symmetrically apart, one grating period per step. For every step, between the two endpoints, the integral of the grating nonlinearity is compared to the integral of the target function. If the grating integral is found to be larger than the target integral, the last reversal is deleted (no domain reversal in that grating period), otherwise the reversal is left alone. The analog target function is thus converted to a digitized QPM

grating, an approach that draws close analogy to the design of $\Delta\Sigma$ A/D converters for integrated circuits. [59] Similar to mode-overlap control, the target function can be freely chosen here.

3.3 Experimental Demonstration

To demonstrate the above amplitude-modulation schemes, we fabricated devices on a 25-mm-long LiNbO$_3$ chip. The RPE waveguides have 3.2-μm-wide mode filters at the input, followed by tapers to widen the waveguides to the 7.5-μm noncritical width. For the double-coupler devices, directional couplers of 1.7-mm length consisting of two 7.5-μm-wide parallel waveguides separated by 2.5 μm are incorporated. The QPM period is 16.10 μm, and the grating lengths L_g are 5.64 mm for mode-overlap-control and deleted-reversal devices, and 3.4 mm for the double-coupler device (twice the coupler length).

Figure 3.4 shows measured SHG tuning curves of QPM gratings using each of the three apodization methods, together with the tuning curve of a uniform grating for comparison. We used three different window functions (all truncated between $-L_g/2 \leq z \leq L_g/2$): $\mathrm{sinc}\,(2\pi z/L_g)$, $\cos^2\,(\pi z/L_g)$, and $e^{-(3.3z/L_g)^2}$, for the mode-overlap-control, double-coupler, and deleted-reversal devices, respectively. In all three apodized cases, the apodization has a clear effect on sidelobe amplitudes. The sidelobes are suppressed to 13-17 dB below the -13-dB characteristic of the first sidelobe of a sinc-square pattern. The contrast approaches the goal of -30 dB with a much smaller detuning than with the uniform grating. Consistent with Fourier transform analysis, apodization has the effects of reducing peak efficiency (not shown) and broadening the main lobe. If they are of concern, apodizing a grating twice as long as the uniform one will fully compensate both effects.

It is useful to define a 30-dB half-bandwidth of a theoretical tuning curve as the maximum detuning that reaches above -30 dB relative to the central peak. For the above studied apodization functions, the 30-dB half-bandwith is close to $\Omega = 5\pi/(\delta\nu L_g)$, compared to $\Omega = 20\pi/(\delta\nu L_g)$ for a uniform grating of the same length. (Ω is the frequency detuning from the phasematching center.) Another figure of
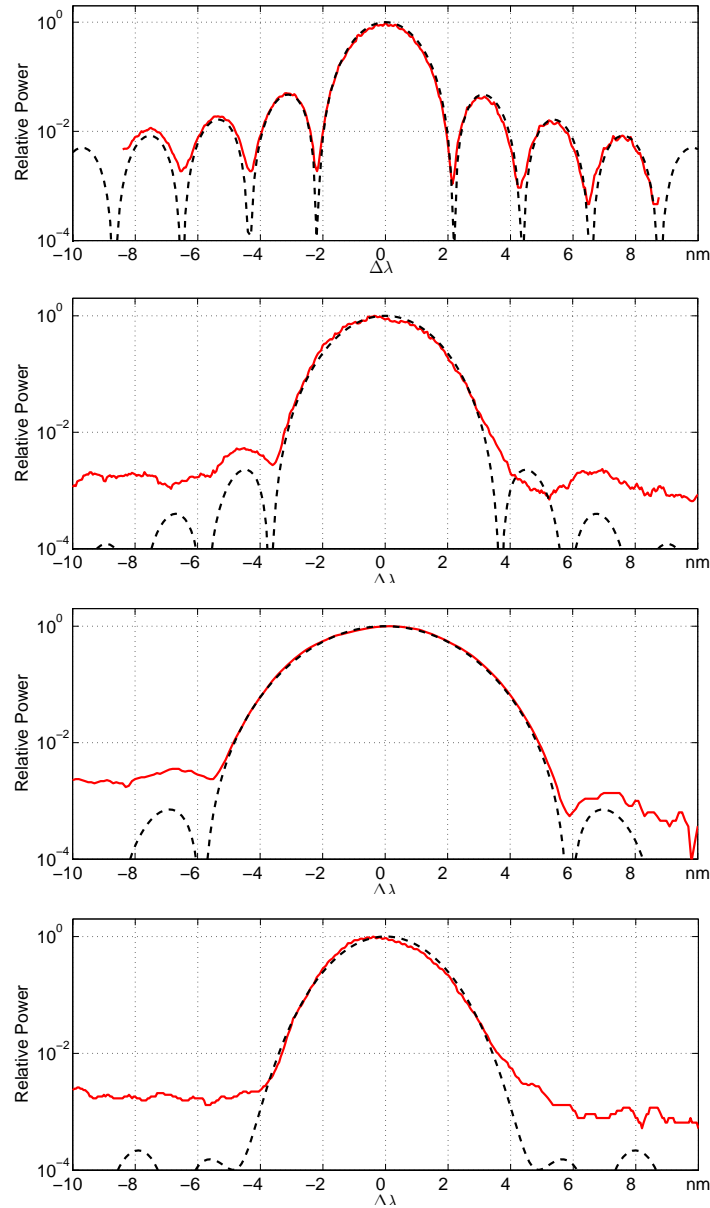
Figure 3.4: The experimental (solid) and theoretical (dashed) SHG tuning curves of a uniform grating and three apodized gratings. From top to bottom: uniform; mode-overlap control; the double-coupler scheme; the deleted-reversal method. In each case, the sidelobes are clearly suppressed with respect to those of the uniform grating. The double-coupler grating is 3.4 mm long, i.e. twice the coupling length, so its tuning curve is wider than that of the 5.64-mm-long gratings in the other three plots.

merit, which is independent of the length of the grating, is the ratio of the 30-dB half-bandwidth to the half width of the main lobe (measured at the first zero in the tuning curve). The ratios are 1.25 and 10 for the apodized and uniform gratings, respectively.

In another set of devices, starting with a 350-period grating apodized according to a cosine-square function, we add different lengths of uniform gratings between the rising and falling edges, as shown in the left column of Figure 3.5. Measuring the tuning curves of these devices we note that the larger the total grating length is, the narrower the main-lobe is, but the higher the side-lobes are. As long as the apodized parts contain the same number of periods, the two effects nearly cancel, so that the 30-dB half-bandwidth is relatively constant for the three cases.

In all gratings studied, the measured tuning curves agree well with theoretical calculations in all but one aspect: their tails reach a floor whose level is roughly $1/N$, where N is the total number of grating periods. This floor limits the extent to which one can benefit from apodization. It also exists for uniform gratings. From numerical simulations, (Figure 3.6) we believe it is the result of random grating duty-cycle errors. A detailed theoretical treatment of this and other types of QPM errors can be found in Ref. [16], whose results are briefly extended to explain this $1/N$ floor in Appendix B. In addition, the tuning behavior of waveguide-based QPM devices is also affected by waveguide inhomogeneities. Interested readers can find a theoretical study of those effects in Appendix A.

3.4 Summary of Chapter 3

We have demonstrated several techniques to modulate the amplitude of QPM interactions. The deleted-reversal devices are the easiest to fabricate, and are not sensitive to alignment errors between gratings and waveguides as the mode-overlap-control devices are. Neither are they sensitive to inaccurate coupler lengths as the double-coupler devices are. Moreover, the deleted-reversal method can be used in bulk devices with modifications that take into account the intensity change due to beam diffraction. However, it may not be suitable for applications involving sub-hundred-femtosecond
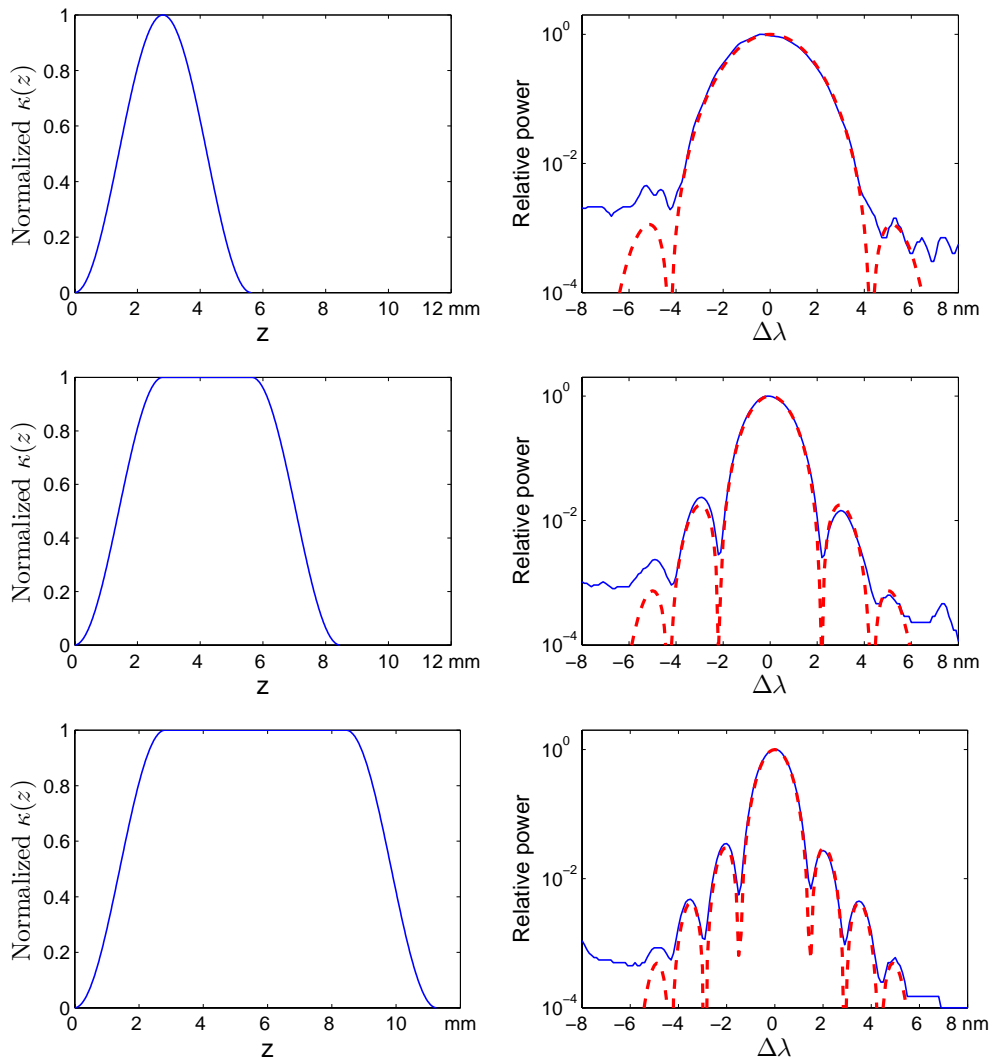
Figure 3.5: $\kappa_1(z)$ profiles (left) and the corresponding tuning curves (right) of three apodized gratings, compared to theoretical calculations (dashed line). In the apodized portion, the three gratings all have 350 QPM periods and use a cosine-square function, but have different lengths of uniform gratings in the middle. The 30-dB bandwidth is relatively constant in the three cases.
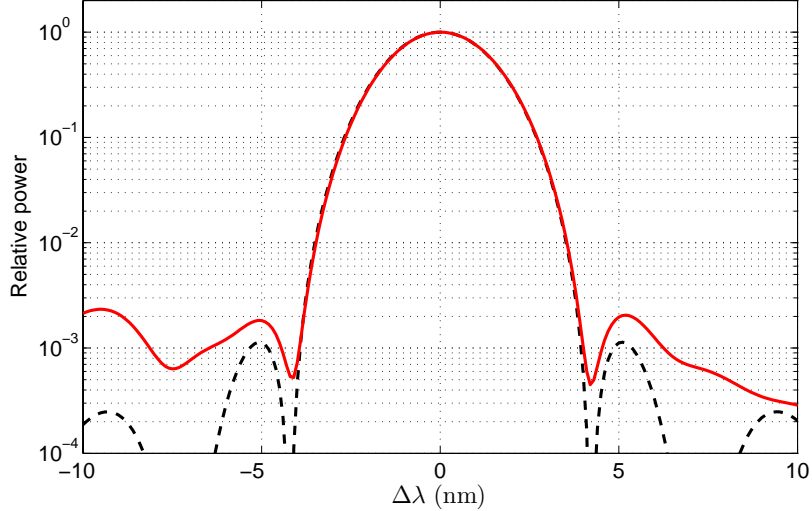
Figure 3.6: The theoretical tuning curve (dashed) of an apodized grating of 350 periods and the simulated curve (solid) with $\pm5\%$-rms normally distributed random error in grating duty-cycles.

pulses, as the walk-off length between FH and SH waves becomes so short that the digitization effects of deleted reversals could manifest. The double-coupler scheme has the advantage of separating the FH and SH light automatically, but unlike the other two methods, the simple design described in this chapter has a fixed cosine-square $\kappa_m(z)$ in the coupler region. However, with more complicated designs, varying the distance between the two waveguides of the coupler for instance, it could also accommodate other target $\kappa_m(z)$ profiles.

The sidelobes of tuning curves have been successfully suppressed by using each of these techniques to apodize the QPM interaction, to the extent that random errors in grating dominate off-phasematching photon generation.

The amplitude modulation techniques developed in this chapter can complement other QPM engineering techniques, such as chirping, duty-cycle variations, phase modulation, etc. Apodizing the amplitude and chirping the periods of a QPM grating simultaneously, for instance, one can achieve a flat gain profile over a wide bandwidth, useful in optical parametric amplification and ultrashort pulse characterization. [60, 61] Application in the latter is described in detail in Ref. [62]. In a wider

context, amplitude modulation is not limited to apodization, but can be used for many other applications that require the alteration of tuning-curve shapes, thereby further extending the functionality of optical signal-processing devices.

Chapter 4

A Monolithic 160-Gbit/s Optical Time-division Multiplexer

4.1 Introduction

An OTDM multiplexer (OTDM-MUX) is a key element of an OTDM system. Multiple data channels are combined by the OTDM-MUX to form the time-sequential OTDM signals. The data can come directly from light sources or from a WDM system. With a 40×4 MUX, four 40-Gbit/s data channels are interleaved into a 160-Gbit/s pulse stream and transmitted at a single wavelength. However, because the pulsewidth of the low-bit-rate data is usually too long to fit in one "bit" of the high-bit-rate system, oftentimes one can not directly delay and combine the data channels to form the OTDM pulse stream. Even if the pulsewidth is appropriate, the timing jitter of the data from the low-bit-rate system tends to be large, and if transferred to the high-bit-rate OTDM stream, will result in interchannel crosstalk. [19, 63]

The requirement for stable multiplexing with minimum fluctuation in pulse separations makes a specific type of OTDM-MUX most promising. Important to the MUX implementation is a gated OF mixer with an optical clock. The optical clock provides a train of short pulses with very low timing jitter, and acts as an optical gate. When they overlap, the clock pulse samples the data pulses and generates a signal pulse through nonlinear frequency mixing. With this gated mixing scheme, the

signals are synchronized to the clock pulses automatically. With jitter in the data, the clock will sample different parts within the data pulses from shot to shot, while the signal timing is not affected. (Figure 4.1)
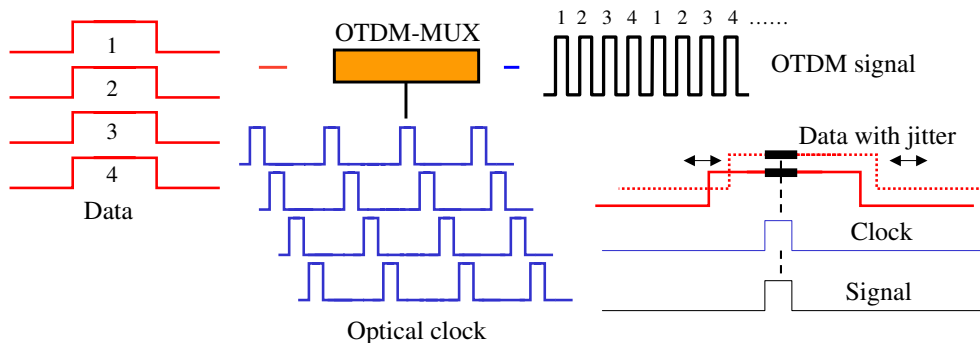
Figure 4.1: OTDM-MUX based on gated mixing. The clock pulses serve as optical gates to sample long data pulses when they overlap.

A 160-Gbit/s OTDM-MUX was previously demonstrated using PPLN waveguides integrated with a planar lightwave circuit (PLC). [18] (Figure 4.2) In that experiment, a 40-GHz optical clock was split by a 1×4 coupler and delayed by four different-path-length PLC delay lines to produce four clock phases. Each clock phase was combined with and modulated by one 40-Gbit/s non-return-to-zero (NRZ) data channel in a separate PPLN waveguide through cascaded SHG/DFG. The four optically modulated signals were then combined by a 4×1 coupler to generate the 160-Gbit/s OTDM signal.

The following functions are essential to an OTDM-MUX:

- a *sampling* mechanism that converts long data pulses to short signal pulses;

- a *timing* mechanism that provides accurate delay to the signals;

- a *multiplexing* mechanism that combines the signals into a pulse stream;

- a *selection* mechanism that distinguishes the signal from unwanted light.

In the PPLN/PLC hybrid MUX, the sampling was through DFG in the PPLN waveguide between a clock pulse and the frequency-doubled data pulse. The different
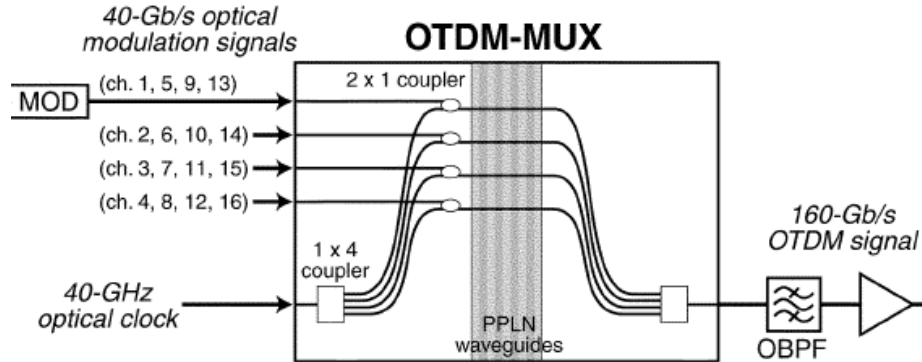
Figure 4.2: A previously demonstrated PPLN/PLC hybrid OTDM-MUX. (Adapted from Ref. [18].)

lengths of PLC delay lines provided accurate timing to each signal channel. The 4×1 coupler combined the signals to form a pulse stream. A bandpass filter selected the signal and discarded light at other frequencies, e.g. the clock, the FH and SH of the injected data. Using the hybrid MUX and a demultiplexer based on semiconductor optical amplifier, 40-Gbit/s × 4 OTDM transmission was successfully demonstrated over 160 km.

Convinced by the advantages of the gated mixing scheme, but unsatisfied with the complicated hybrid design, we have developed a monolithic MUX fabricated entirely on a single PPLN substrate. It is capable of 40-Gbit/s × 4 operation. By tailoring and integrating multiple optical signal-processing functions on a single substrate, we are able to use one instead of four PPLN waveguides and eliminate the use of additional couplers and silica-on-silicon circuitry, hence achieving a monolithic layout and higher efficiency, while keeping the crosstalk low. I describe the MUX scheme in Section 4.2. This is followed in Section 4.3 by the relevant theory to evaluate the MUX performance. In Section 4.4 I present experimental characterization of the device using ultrafast optical techniques. I hope readers will find interesting and useful not only the demonstration of the MUX, but also the various experimental techniques we used to test the device. They are readily transferable to other applications. Further discussion and proposed future work are presented in Section 4.5.

4.2   The Monolithic Multiplexer Scheme

The PPLN MUX is shown schematically in Figure 4.3. The first part of the MUX converts an external 40-GHz FH clock to a four-phase SH clock: Each new clock pulse now consists of four discrete frequencies overlapped in the time domain. Next, the four-phase clock and four channels of data are injected into the sampling gratings. There they mix in four different grating segments, which also provide the necessary time delays between channels. The generated OTDM signals pass the bandpass filter at the output. This section describes the working principles of each functional part.
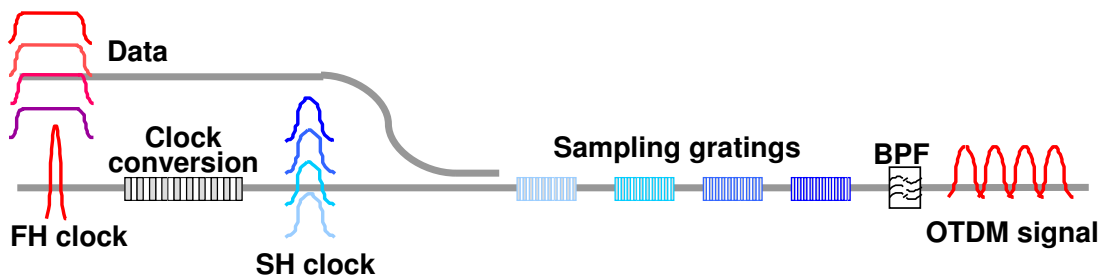
Figure 4.3: Schematic of the PPLN MUX, consisting of a clock-conversion part and a sampling part.

4.2.1   Clock conversion in phase-modulated gratings

The MUX takes as input an external clock in the C band. The repetition rate of the external clock should match the bit rate of each data channel (40 Gbit/s). Large bandwidth is also required for the generation of four spectrally distinct SH clock phases.

From the external FH clock, a SH clock is generated in the QPM grating through SHG. Observed in the time domain, the new clock remains a 40-GHz pulse train. It is the frequency-domain picture of the clock that has some important new features: (1) Each clock pulse now exhibits four discrete frequency peaks; (2) the peaks are at SH frequencies. We can view the new clock as four perfectly synchronized 40-GHz clocks with four different "colors", and they become the four phases of a 160-GHz

clock. These spectral features are important to the timing and selection mechanisms of the MUX, as we will see shortly in Section 4.2.2. In this section I shall explain how to generate such a clock with desired properties.

Recalling Eq.(1.11) and the discussion in Section 1.2.1, a QPM grating is a frequency-domain nonlinear filter. With a broadband input, the SH spectrum is proportional to the grating transfer function. A uniform QPM grating has the familiar sinc transfer function with a single center peak. In order to generate the four clock phases, we need a QPM grating that has four peaks in its transfer function.

QPM gratings with multiple transfer-function peaks have proved useful for multi-channel wavelength converters in WDM applications, [7, 49] and for improving the temporal properties of the output of a pulsed OPA. [64] To date, several domain structures have been proposed, including a periodic-phase-reversal structure [7], a superlattice structure [50], an aperiodic poling structure, [51] and a phase-modulated structure. [49] The phase-modulation approach has several advantages, such as versatile control over peak amplitudes and positions, loosest fabrication requirements, and minimum loss in efficiency.

Phase modulation is realized by periodically shifting the center positions of the domains with a phase-modulation period Λ_{ph}, as illustrated in Figure 4.4. Within each phase period, the domains are shifted according to a phase-modulation function. The simplest functional form is $+\pi$ for the first half period and $-\pi$ for the second half. [7] This phase-reversal grating produces two first-order QPM peaks of the same amplitude. More complicated phase-modulation functions can be designed to obtain desired tuning curves.
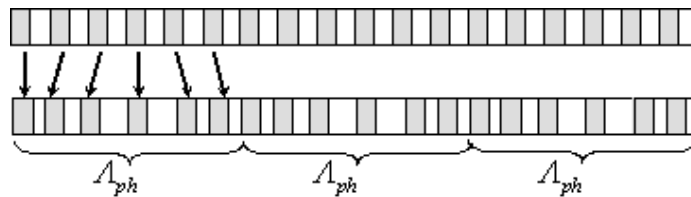
Figure 4.4: Schematic of a phase-modulated QPM grating.

From the Fourier-transform analysis we gain insights that help to design the different aspects of the phase-modulated grating:

1. Λ_{ph} determines the peak separation. The QPM grating has spectral peaks when the wavevector mismatch satisfies

$$\Delta k = 2\pi \left(\frac{1}{\Lambda_0} + \frac{m}{\Lambda_{\mathrm{ph}}} \right), \tag{4.1}$$

where Λ_0 is the average QPM period and m is an integer. From Eq.(4.1) Λ_{ph} can be related to design parameters by

$$\Lambda_{\mathrm{ph}} = \frac{\omega_2}{\Delta\omega_2}\Lambda_0, \tag{4.2}$$

where ω_2 is the SH phasematching frequency that corresponds to Λ_0 and $\Delta\omega_2$ is the separation of QPM peaks at the SH frequency. Given desired center frequency and QPM peak separation, one first chooses Λ_{ph} using Eq.(4.2).

2. The functional form of the phase modulation controls the ratio of the heights of the transfer function peaks. In order to have equal power in the four clock phases, the finite bandwidth of the FH clock must be compensated by making the two center peaks of the tuning curve smaller than the two side peaks. The actual ratio depends on the spectrum of the FH clock and the frequency spacing of the SH clock phases. The phase-modulation function is generated by iterated numerical optimization until its Fourier spectrum has the required peak amplitude ratios. Figure 4.5 shows several phase-modulation functions and the corresponding tuning curves.

3. The width of individual peaks is inversely proportional to the total length of the grating, and is similar to the bandwidth of a uniform grating of the same-length. The area under the first-order peaks is typically 90% that of a uniform grating of the same length.

In the phase-modulated grating, the broadband FH pulses of the external clock are doubled to the SH, with a spectrum given by the grating transfer function filtering the spectrum of the squared pump pulse. In the time domain, as a result of GVM, the pulse is broadened to roughly $\tau = \delta\nu L_{\mathrm{cg}}$, where $\delta\nu$ is the GVM parameter and
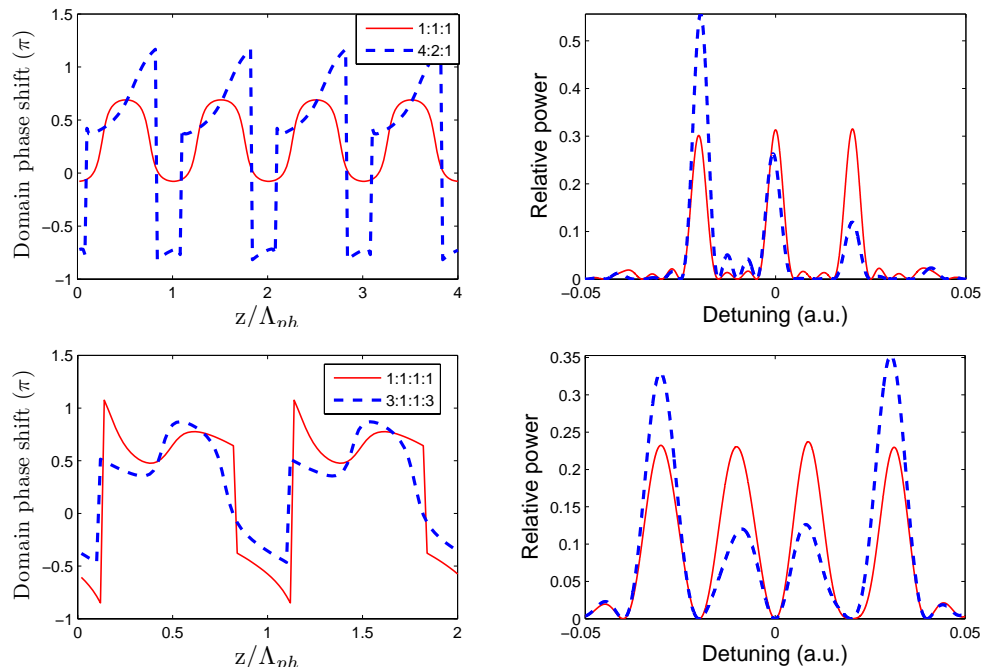
Figure 4.5: Phase-modulation functions (left) and the corresponding tuning curves (right). Note the peak width, spacing and ratios are controlled by the grating length, modulation period, and functional form, respectively.

L_{cg} is the length of the clock-conversion grating. This is equivalent to the grating's nonlinear filtering effect that narrows the spectrum of each clock phase.

4.2.2   Sampling, timing, and selecting

The four-phase clock now enters the sampling part of the MUX, consisting of four segmented sampling gratings, each of length L_{sg} and center-to-center separation L_u. The QPM periods Λ_i of the sampling gratings are chosen such that the carrier frequency of the ith clock phase equals the SH phasematching frequency of the ith sampling grating.

Now suppose only channel 1 data is switched on. In the ith sampling grating, only the ith clock phase falls within the pump bandwidth of that grating (the ith grating "sees" just the ith clock phase), and the difference frequency between the ith clock phase (at frequency ω_{p1}) and channel 1 data (at frequency ω_{d1}) is generated at $\omega_{p1} - \omega_{d1}$. A channel-1-data pulse mixes with a different clock phase in each sampling grating. Altogether, it generates four pulses at four different frequencies. If we choose a bandpass filter at the output of the device that passes just $\omega_{p1} - \omega_{d1}$, viewed after the filter the other three pulses can be neglected in the analysis of the device.

When all four data channels are present, each generates four signal pulses. The frequencies of the sixteen pulses form a matrix $\omega_{pi} - \omega_{dj}$. Elements in the same column are generated in the same sampling grating and elements in the same row are from the same data channel. If the frequency-domain spacing of SH clock phases and data channels are the same, all diagonal elements are equal in frequency. A bandpass filter at that common frequency selects just those four pulses. (Tab. 4.1)

The timing of the four pulses is the direct consequence of each pulse being generated in a different grating. Each signal pulse is synchronized to the SH clock pulse the moment it is generated. Thereafter, due to GVM between the C-band signal and SH clock, the signal pulse leads the clock pulse by $\delta\nu l$ as it propagates a distance l. Therefore the signal pulse generated in an earlier grating leads the next one by $\Delta t = \delta\nu L_u$. In a 160-Gbit/s system $\Delta t = 6.25$ ps. Given $\delta\nu = 0.36$ ps/mm in PPLN waveguides, we need $L_u = 17.36$ mm. In Chapter 2 GVM was compensated

	SG I	SG II	SG III	SG IV
Ch 1	$\omega_{p1} - \omega_{d1}$	$\omega_{p2} - \omega_{d1}$	$\omega_{p3} - \omega_{d1}$	$\omega_{p4} - \omega_{d1}$
Ch 2	$\omega_{p1} - \omega_{d2}$	$\omega_{p2} - \omega_{d2}$	$\omega_{p3} - \omega_{d2}$	$\omega_{p4} - \omega_{d2}$
Ch 3	$\omega_{p1} - \omega_{d3}$	$\omega_{p2} - \omega_{d3}$	$\omega_{p3} - \omega_{d3}$	$\omega_{p4} - \omega_{d3}$
Ch 4	$\omega_{p1} - \omega_{d4}$	$\omega_{p2} - \omega_{d4}$	$\omega_{p3} - \omega_{d4}$	$\omega_{p4} - \omega_{d4}$

Table 4.1: Generated signal frequencies, assuming four data channels at ω_{di}, $i = 1 - 4$; four SH clock phases at ω_{pj}, $j = 1 - 4$. As long as the data channel spacing in the frequency domain equals the clock phase spacing, the diagonal elements are equal and can be selected by a bandpass filter.

to achieve higher bandwidth/efficiency product; here it is exploited as a convenient delay mechanism to set correct signal timing. Since $\delta\nu$ and L_u are both fixed, the timing is as accurate as the clock itself. These processes are illustrated in Figure 4.6.
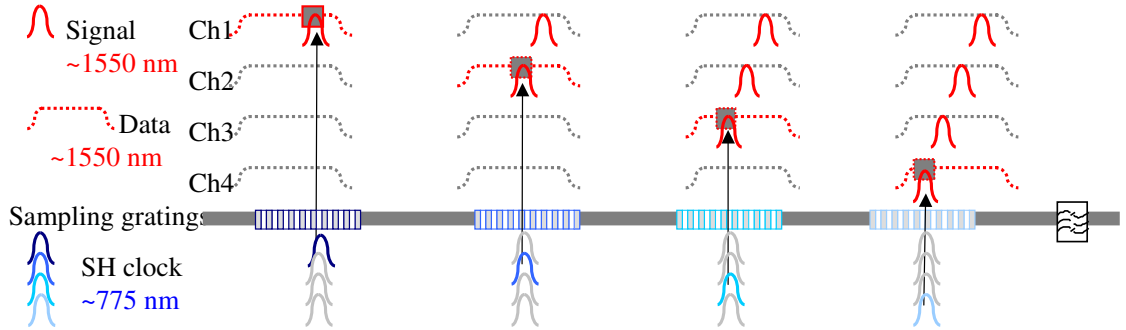
Figure 4.6: Illustration of signal timing. A signal pulse is generated in the grating corresponding to a certain data/clock-phase pair. Immediately after, the signal starts to walk off from the clock. The delay between two signal pulses generated in two gratings is determined by GVM and the separation of the gratings.

If the transfer functions of the sampling gratings partly overlap, the four signal pulses from the same row of Tab. 4.1 are not truly distinct in the frequency domain, and a fraction of the pulse energy will pass the bandpass filter, becoming interchannel crosstalk. To minimize crosstalk, one can apodize the sampling gratings to suppress transfer function sidelobes, by using the techniques developed in Chapter 3.

4.3   Theoretical Treatment

The nonlinear optical process on which the OTDM-MUX is based is cascaded SHG/DFG in two separate gratings, with the SH of the external clock serving as the pump of the subsequent DFG step in the sampling gratings. The carrier frequencies of the OTDM signal (ω_s), the SH clock (ω_p), and data (ω_d) satisfy $\omega_s = \omega_p - \omega_d$. (Data and OTDM signal correspond to the signal and idler, respectively, in the conventional terms of a DFG process.) Under the undepleted pump, unamplified signal, and no-loss limit, the transfer functions for these processes are given by Eqs.(1.11) and (1.23) in Section 1.2.1. Because the data bandwidth ($\sim 10^{10}$ Hz) is sufficiently narrow compared to the pump bandwidth ($\sim 10^{12}$ Hz) of each sampling grating (equivalently the data walk-off length is much longer than the sampling grating), the frequency-domain envelope of the data can be approximated as a delta function, i.e. $\hat{A}_d = a_d \delta(\omega = \omega_d)$, and Eq.(1.23) is simplified to Eq.(1.26). The signal spectrum is limited by the bandpass filter at the output. Summarizing the above discussions, for a given data channel (we have chosen data channel 2 for the following discussions), we obtain:

$$\hat{A}_{\text{os}}(\Omega) = f(\Omega)\hat{D}_{\text{sg}}(\Omega)\hat{D}_{\text{cg}}(\Omega)\widehat{A_{\text{cl}}^2}(\Omega)a_d \tag{4.3}$$

Ω is the frequency detuning from ω_s and ω_p. $f(\Omega)$ is the bandpass filter function, and $\hat{A}_{\text{os}}(\Omega)$ is the frequency-domain field envelope of the OTDM signal. $\widehat{A_{\text{cl}}^2}(\Omega)$ is the self-convolution of the external clock's frequency-domain envelope, defined in Eq.(1.13). $\hat{D}_{\text{cg}}(\Omega)$ is the SHG transfer function of the clock-conversion grating and $\hat{D}_{\text{sg}}(\Omega)$ is the sum of the DFG transfer functions of the four sampling gratings:

$$\hat{D}_{\text{sg}}(\Omega) = \sum_{m=-1}^{2} \hat{D}_{\text{DFG}}(\Omega + m\Delta\omega_d)e^{-i\delta\nu(\Omega+m\Delta\omega_d)mL_u} \tag{4.4}$$

where $\Delta\omega_d$ is the frequency-domain data channel spacing. The numbering of m from -1 to 2 results from our choice of data channel 2 as the reference point, where $m = 0$. The phase term comes from the grating position and the Fourier shift theorem. $\hat{D}_{\text{cg}}(\Omega)$ and $\hat{D}_{\text{DFG}}(\Omega)$ are explicitly defined in Eqs. (1.12) and (1.27).

To generate four equal amplitude SH clock phases from a FH pump with limited

bandwidth, the clock-conversion grating was designed to have a transfer function with two outer spectral peaks larger than the inner peaks. In addition, the peak positions of $\hat{D}_{sg}(\Omega)$ are designed to match those of $\hat{D}_{cg}(\Omega)$. (Figure 4.7a) The spectrum resulting from the mixing of this SH clock and one data channel is shown in Figure 4.7b. After the bandpass filter, only one lobe is selected, and the contributions from the tails of $\hat{D}_{\mathrm{DFG}}(\Omega + m\Delta\omega_d)(m \neq 0)$ become crosstalk in the corresponding time slots. (Figure 4.7c).
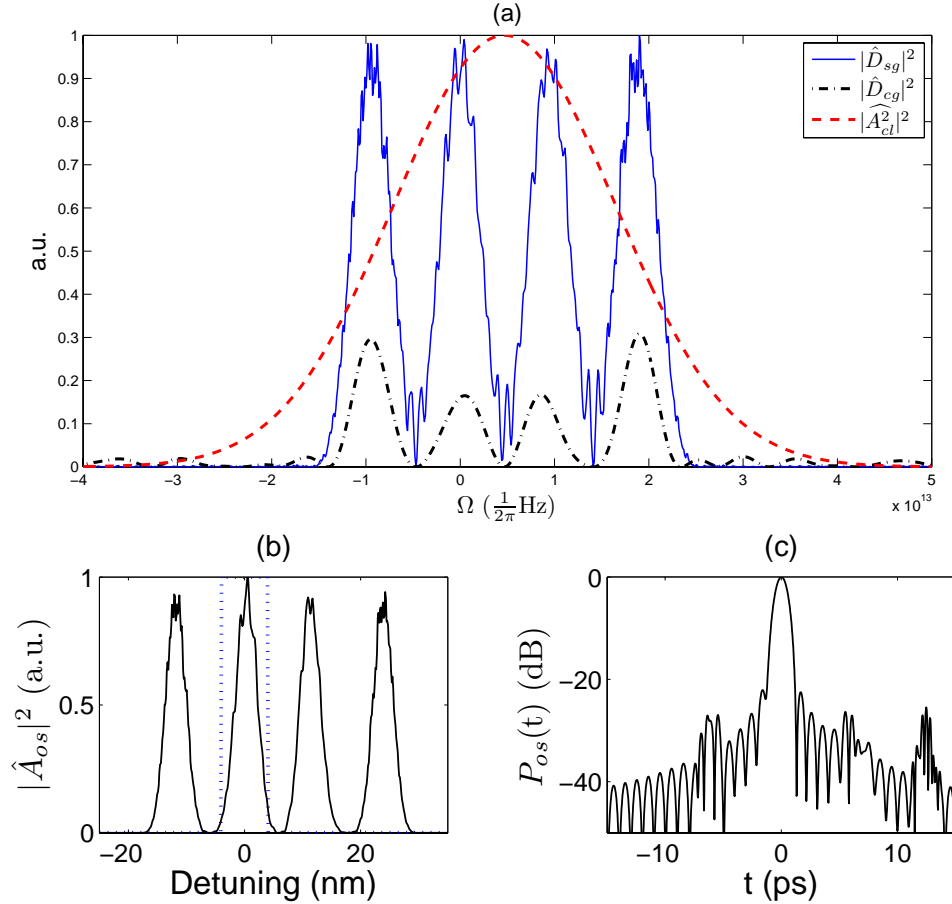
Figure 4.7: a: the grating transfer functions and spectrum of the external clock; b: signal spectrum (solid) after data-clock mixing and before the bandpass filter (dashed); c: signal pulse shape in time domain.

The energy in the OTDM signal pulse is:

$$U_{\text{os}} = \int_{-\infty}^{\infty} \left| \hat{A}_{\text{os}}(\Omega) \right|^2 \, d\Omega = P_d \int_{-\infty}^{\infty} \left| f(\Omega)\hat{D}_{\text{cg}}(\Omega)\hat{D}_{\text{sg}}(\Omega)\hat{A}_{\text{cl}}^2(\Omega) \right|^2 \, d\Omega, \qquad (4.5)$$

where P_d is the peak input data power. We use the following normalizations to relate U_{os} to the normalized efficiency η_{nor} of a PPLN grating:

For the phase-modulated clock-conversion grating:

$$\left| \hat{D}_{\text{cg}}(\Omega) \right|^2 = \eta_{\text{nor}} L_{\text{cg}}^2 \left| \bar{D}_{\text{cg}}(\Omega) \right|^2 \qquad (4.6)$$

The sum of the four peak heights of $\left| \bar{D}_{\text{cg}}(\Omega) \right|^2$ is unity.

For a sampling grating apodized according to a cosine-square function, its peak efficiency is 1/4 that of a uniform grating of the same length, so

$$\left| \hat{D}_{\text{sg}}(\Omega) \right|^2 = \frac{\eta_{\text{nor}}}{4} L_{\text{cg}}^2 \left| \bar{D}_{\text{sg}}(\Omega) \right|^2 \qquad (4.7)$$

where each of the four peaks of $\left| \bar{D}_{\text{sg}}(\Omega) \right|^2$ is unity.

$\hat{A}_{\text{cl}}(\Omega)$ can be written as

$$\hat{A}_{\text{cl}}(\Omega) = \hat{A}_{\text{cl}}(0)\bar{A}_{\text{cl}}(\Omega) \qquad (4.8)$$

where the peak of $\bar{A}_{\text{cl}}(\Omega)$ is unity. $\bar{D}_{\text{cg}}$, $\bar{D}_{\text{sg}}$, and $\bar{A}_{\text{cl}}$ are unitless. The energy in the clock pulse is

$$\int_{-\infty}^{\infty} \left| \hat{A}_{\text{cl}}(\Omega) \right|^2 \, d\Omega = b \left| \hat{A}_{\text{cl}}(0) \right|^2 = \frac{P_{\text{cl}}}{r_{\text{bit}}}, \qquad (4.9)$$

where P_{cl} is the average clock power and r_{bit} is the bit rate of data and clock, and

$$b = \int_{-\infty}^{\infty} \left| \bar{A}_{\text{cl}}(\Omega) \right|^2 \, d\Omega. \qquad (4.10)$$

So

$$\hat{A}_{\text{cl}}(0) = \sqrt{\frac{P_{\text{cl}}}{br_{\text{bit}}}}. \qquad (4.11)$$

If we assume a Gaussian clock pulse with $1/e$ half bandwidth $\Delta\Omega_{\rm cl}$:

$$\bar{A}_{\rm cl}(\Omega) = e^{-\frac{\Omega^2}{\Delta\Omega_{\rm cl}^2}}, \tag{4.12}$$

then $b = \sqrt{\frac{\pi}{2}}\Delta\Omega_{\rm cl}$. If the Gaussian pulse is transform limited and has a FWHM duration $\tau_{1/2}$, then $b \approx 2.1/\tau_{1/2}$.

With Eqs. (4.5) through (4.11), we have

$$U_{\rm os} = P_d \left(\frac{\eta_{\rm nor}L_{\rm cg}L_{\rm sg}P_{\rm cl}}{2br_{\rm bit}}\right)^2 \int_{-\infty}^{\infty} \left|f(\Omega)\bar{D}_{\rm cg}(\Omega)\bar{D}_{\rm sg}(\Omega)\overline{A_{\rm cl}^2}(\Omega)\right|^2 d\Omega \tag{4.13}$$

where $\overline{A_{\rm cl}^2}(\Omega)$ is the self-convolution of $\bar{A}_{\rm cl}(\Omega)$. Note that the overall transfer function gets narrower with larger $L_{\rm cg}$ and $L_{\rm sg}$, so the signal pulse energy does not scale with $(L_{\rm cg}L_{\rm sg})^2$ in general.

Define the MUX efficiency as the ratio of signal to data pulse energy normalized to the square of average clock power:

$$\eta_{\rm MUX} \equiv \frac{U_{\rm os}}{U_d P_{\rm cl}^2} = \frac{1}{r_{\rm bit}}\left(\frac{\eta_{\rm nor}L_{\rm cg}L_{\rm sg}}{2b}\right)^2 \int_{-\infty}^{\infty}\left|f(\Omega)\bar{D}_{\rm cg}(\Omega)\bar{D}_{\rm sg}(\Omega)\bar{A}_{\rm cl}^2(\Omega)\right|^2 d\Omega \tag{4.14}$$

In the last relation we have assumed NRZ data format so that $U_d \approx P_d/r_{\rm bit}$. Although the loss of a long PPLN device is not negligible, Eq.(4.3) is still a good approximation, because $L_{\rm cg} + L_{\rm sg}$ is short and the loss in that region is below 0.5 dB. The true signal pulse energy and MUX efficiency are modified by a simple propagation loss term $e^{-(\alpha_1 L_1 + \alpha_2 L_2)}$, where α_1 and α_2 are the power loss coefficients at the FH and SH frequencies, and L_1 and L_2 are the propagation distance of the OTDM signal and SH clock, respectively.

There are two separate origins of crosstalk. First, without considering adjacent sampling gratings, in the time domain the generated signal pulse has tails that extend into other time slots. Second, crosstalk comes from the tails of the transfer function $\hat{D}_{\rm DFG}(\Omega + m\Delta\omega_d)(m \neq 0)$ at the filter pass band around $\Omega = 0$. The latter is reduced but not eliminated by apodization. To evaluate the total effect, we take the overall spectrum calculated with Eq.(4.3) and Fourier transform it to get the time-domain

pulse envelope, i.e. $P_{os}(t) \propto \left| \int_{-\infty}^{\infty} \hat{A}_{os}(\Omega) e^{i\Omega t} d\Omega \right|^2$. The crosstalk from each channel is quantified as

$$X = \frac{\int_{T/2}^{3T/2} P_{os}(t)\, dt}{\int_{-T/2}^{T/2} P_{os}(t)\, dt}, \tag{4.15}$$

where T is the duration of one bit (6.25 ps in a 160-Gbit/s system). This crosstalk is "in-band", meaning that the crosstalk from all channels is coherent and adds up interferometrically. From a system point of view, the acceptable crosstalk level is $X < -26$ dB [54] if we assume that crosstalk comes only from adjacent channels. If ultrafast ($>>$ 160 GHz) phase scrambling of data channels is available, this requirement is loosened to $X < -20$ dB. [55]

Given the data channel spacing, which determines Λ_{ph}, one needs to choose the number of phase-modulation periods, hence L_{cg}, the length of each sampling grating, L_{sg}, and the filter function $f(\Omega)$. Without an analytical expression for $\hat{A}_{os}(\Omega)$ optimizing the parameters in the most general form for both efficiency and crosstalk is difficult. However, with Eqs. (4.14) and (4.15) numerical evaluation of the efficiency and crosstalk is straightforward. In this way we compare the MUX performance to theory in the next section.

4.4 Experimental Demonstration

4.4.1 Device

To demonstrate the OTDM-MUX, we fabricated the device using PPLN RPE waveguides. The input section of the device is a 3-μm-wide mode filter followed by a quadratic taper to widen the waveguide to the 6.5-μm noncritical phasematching width. Between the clock-conversion grating and first sampling grating, there are two wavelength-selective directional couplers. Each coupler is 1.5-mm long, consisting of two parallel 6.5-μm-wide waveguides separated by 2 μm. The first coupler is an ω-remover to filter out the external FH clock; the second one couples data into the MUX.

As was discussed in Section 4.2.2, for correct signal timing, we need $L_u = 17.36$

mm. With this constraint the sampling part alone is longer than 58 mm. Including the input and clock-conversion sections, the total device length exceeds 70 mm. In order to fabricate the device on a chip diced from a 3-inch-diameter (76 mm) wafer, we integrated a 180-degree bend to use twice the chip length. With a 2.39-μm initial proton-exchange depth, 23-hr annealing at 310 °C, and 27-hr RPE at 300.5 °C, the minimum bend radius with negligible bending loss is 2 mm. Now that the clock and data input, and signal output ports are at the same end of the chip, they are spaced by 250 μm to align with three optical fibers of a V-groove array. The device, shown (not to scale) in Figure 4.8, has a tennis-racket shape.
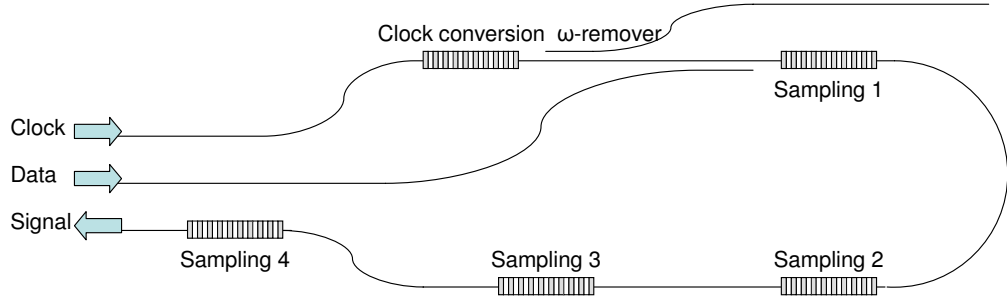
Figure 4.8: Schematic of the MUX integrated on a single chip.

In the proof-of-principle device, the clock-conversion grating has a total length of 4.47 mm with two phase-modulation periods. The average QPM period is 14.80 μm. It is aimed for a data channel spacing of 11.5 nm. The peak ratios of the tuning curve are designed to be 1.8:1:1:1.8 to compensate for the 25-nm FWHM of the external clock and generate four clock pulses of equal amplitude at 770.5, 773.3, 776.0 and 778.8 nm. Each sampling grating is 5.18-mm long, with local nonlinear coupling apodized according to $\kappa(z) \propto \cos^2\left(\pi z/L_{\mathrm{sg}}\right)$ ($z = 0$ is grating center) using the deleted-reversal technique. The grating periods are 14.56, 14.68, 14.80 and 14.92 μm to match the wavelengths of the four-phase clock.

4.4.2   Apparatus

Figure 4.9 shows the experimental setup. The 150-fs C-band pulses of the external clock came from an optical parametric oscillator (Spectra-Physics OPAL) pumped by a mode-locked Ti:sapphire laser (Spectral-Physics Tsunami). It had an 82-MHz repetition rate. Before coupling into the clock port of the MUX, the pulses went through carefully balanced lengths of single-mode and dispersion-compensating fibers to maintain the pulse width. The data was from a tunable CW laser amplified by an EDFA. The PPLN chip was held at 100 °C to protect it from photorefractive damage. The 10-skip-0 filter at the output had a passband center at 1549.8 nm, an 8-nm 0.5-dB bandwidth, and a 9-nm 30-dB bandwidth. The signal was connected to an optical spectrum analyzer (OSA) for frequency-domain measurements and a cross-correlator for time-domain characterizations.
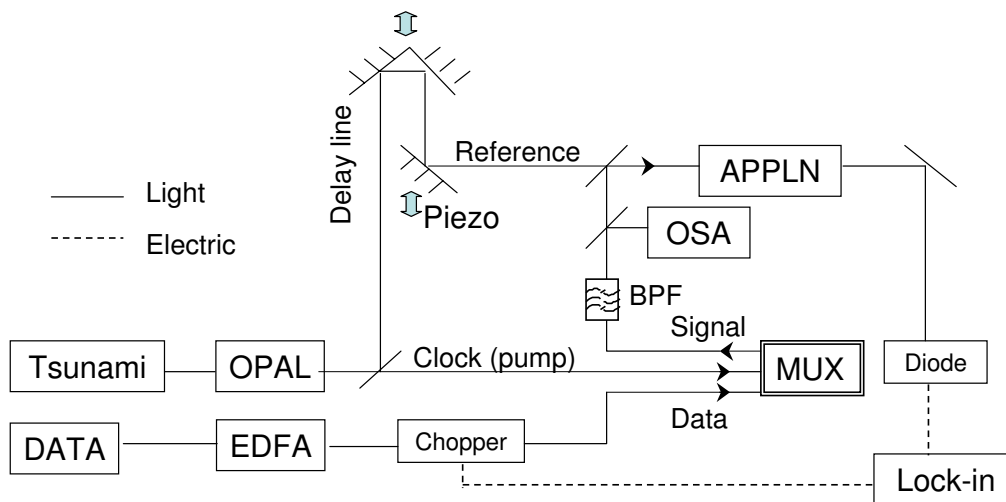
Figure 4.9: The experimental setup for OTDM-MUX characterizations.

The cross-correlator took 10% of the external clock power as a reference for cross-correlation with the output pulses. The approximately 3-meter path lengths of the reference and the signal were carefully adjusted to match (within 5-mm difference). A delay line periodically changed the reference path length so that in time domain, it swept through 50 ps and overlapped with a signal pulse for a fraction of each period.

For cross-correlation, the reference and signal were both injected into an aperiodically poled lithium niobate (APPLN) waveguide, [10] in which SFG took place when the two pulses overlapped. The longitudinally chirped QPM periods provided enough SFG bandwidth for undistorted cross-correlation. The time-resolved SFG power was proportional to the convolution of the two pulses' time-domain power envelopes. When the reference pulse was narrow enough to be approximated as a delta function in the time domain, the signal pulse envelope was obtained directly. Due to the high nonlinear efficiency of the APPLN-waveguide mixer, this cross-correlator was 10^3 times more sensitive than a earlier-version cross-correlator using two-photon processes in a GaAsP photodiode. [65] A similar technique has been used elsewhere to demonstrate autocorrelation and frequency-resolved optical gating (FROG) of hundred-aJ pulses. [60, 61]

To keep the clock, data, and signal all in the C band, their frequencies cannot be too far apart. That constraint resulted in the APPLN chip also efficiently generating the SH of the reference pulse. Much of the wide bandwidth of the SFG light (of the signal-reference cross-correlation) and SHG light (of the reference) overlapped: they could not be distinguished with a spectrophotometer. Due to the high peak power of the reference pulses, the SHG was overwhelming. To overcome this difficulty, we chopped the data input at 1.5 kHz. Consequently, the OTDM signal, and hence the SFG but not the SHG light, was modulated at the same frequency, and was selectively detected by a lock-in amplifier.

In the experimental MUX, due to the non-ideal ω-remover, a small amount of the external clock (pump) power leaked into the output. Although neither the pump nor the reference was chopped, the interferometric cross-correlation of the two was still detected by the lock-in amplifier, introducing noise into the measurement. There were two mechanisms that accounted for this behavior. First, in the MUX, through thermal effects, the data power changed the phase of the residual pump in the same waveguide at the chopping frequency, and the phase change translated into power fluctuation through interference with the reference. Second, even when no data was present, air flow in the 3-m-long light path randomly modulated the relative phase of the interfering light. The phase-modulated interference patten exhibited a wide range

of local frequencies, which inevitably had a component at the chopper frequency. We used the phase dithering method [66] to solve the problem: A piezo-actuated mirror provided exactly 2π phase change at 10 kHz to the reference beam, so that any lower frequency phase modulation did not change the power averaged at the chopper frequency.

4.4.3   Characterization
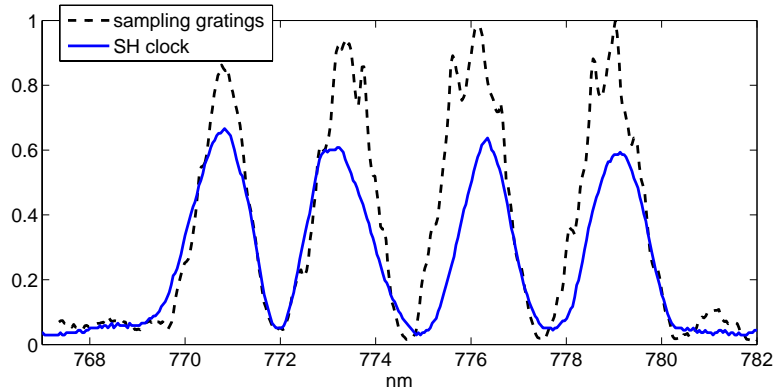
Figure 4.10: Spectral-domain characterization. Overlap of the SH-clock spectrum (solid) and sampling-grating transfer function (dashed) is critical to the integrated operation.

We started with the spectral domain characterization of individual components of the device. Measured with an OSA, the solid curve in Figure 4.10 confirms that the four phases of the SH clock had approximately equal energy. The dashed CW tuning curve of the four-segment sampling grating is proportional to $\left|\hat{D}_{\mathrm{sg}}\right|^2$. Plotted together, the curves confirm that the SH clock wavelengths matched the sampling gratings' pump acceptance bands. This was critical to the successful operation of the integrated device. The absolute spacing of the SH clock phases corresponds to an 11-nm data channel spacing.

Although the sampling gratings were apodized and each had <-30-dB tuning-curve sidelobes, one should not be surprised to see the fringes on the tuning-curve peaks. In the CW measurement, the SH waves generated in all the gratings were

coherent, and at any given wavelength they combined interferometrically. A -30-dB power contribution from an adjacent grating can account for $\pm 7\%$ power fluctuation at the peaks. This fluctuation is also seen in the theoretical curve in Figure 4.7.
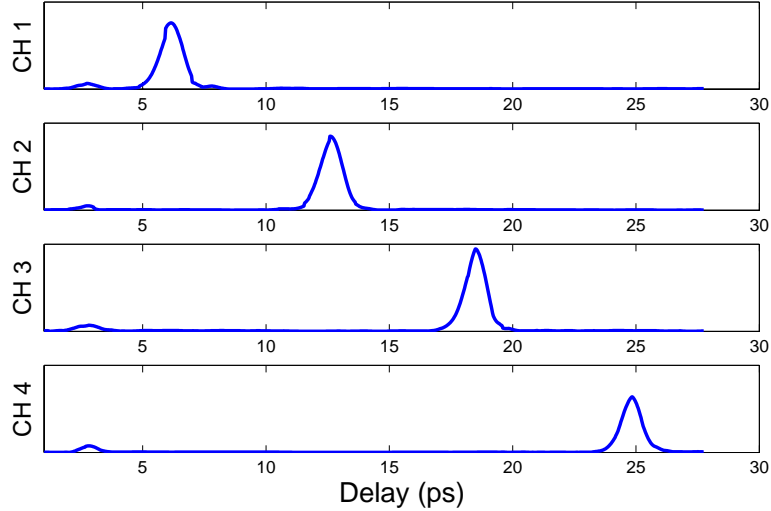
Figure 4.11: Time-resolved OTDM signal power from four data channels, measured with a cross-correlator.

The integrated device was characterized in the time domain. The CW laser was tuned to 1532.2 nm, 1543.2 nm, 1554.2 nm, and 1565.2 nm to simulate data channels 1–4. The OTDM signals from the four channels are shown in Figure 4.11. The small peaks to the left of each plot are a result of the residual pump pulse filtered by the bandpass filter. They serve as markers in the time-domain traces. With 1-mW average clock power and 60-mW data power coupled into the MUX, the OTDM signal power was 9–14 μW for the four channels. If the clock were scaled from 82 MHz to 40 GHz at the same pulse energy, the corresponding efficiency would be 35-50%/W^2. A major obstacle in the experiments was the low average signal power due to the low clock repetition rate, roughly 1/500 that of a real system. However, with the highly efficient APPLN cross-correlator, we were still able to achieve a signal-to-noise ratio exceeding 20 dB. The electronic noise of the lock-in amplifier and the 1/f noise of the reference light each accounted for about half of the remaining noise floor. Short of a system test, the ultafast characterization revealed most key aspects of the MUX,

e.g. timing accuracy, data channel spacing, pulse shape, efficiency and crosstalk. Measured MUX performance is compared to theoretical calculations in Tab. 4.2.

	$\Delta\lambda_{\mathrm{data}}$(nm)	T (ps)	τ (ps)	X(dB)	η_{MUX}(%/W^2)
Design	11.5	6.25	1.7	-27	68
Real device	11	6.2	1.5	<-20	35-50

Table 4.2: Calculated and measured MUX performance. τ is the FWHM of signal pulses. Theoretical efficiency calculated with 3-dB propagation loss. Measured efficiency has been scaled to 40 Gbit/s.

4.5   Further Discussion

We first compare in Tab. 4.3 the different MUX mechanisms in the monolithic and hybrid designs.

	PPLN/PLC hybrid MUX	PPLN monolithic MUX
Sampling	DFG (SH of data as pump)	DFG (SH of clock as pump)
Timing	PLC waveguides	GVM in PPLN waveguide
Multiplexing	4×1 couplers	WDM couplers
Selection	bandpass filter	bandpass filter and ω-remover

Table 4.3: Comparing the different MUX mechanisms of the hybrid and monolithic designs. For the multiplexing mechanism, power is wasted in the 4×1 couplers, while the WDM couplers are theoretically lossless.

We have characterized the integrated operation of the OTDM-MUX using ultra-fast optical techniques, and its performance agreed well with theory. It has several advantages over the hybrid MUX. The monolithic design simplifies fabrication processes. The delay mechanism that makes use of GVM eliminates the use of several couplers and greatly reduces the number of waveguides. Although a band of colors were generated in the MUX, the selection mechanism worked well and crosstalk was not an issue. The proof-of-principle device we demonstrated in this chapter already had a slightly higher efficiency compared to 32%/W^2 in Ref. [18]. With an optimized design, the data channel spacing can be reduced and efficiency improved by using

either longer clock-conversion gratings or longer sampling gratings, or both, as the below numerical example shows.

$\Delta\lambda_{\text{data}}(\text{nm})$	$L_{\text{cg}}(\text{mm})$	$L_{\text{sg}}(\text{mm})$	$X(\text{dB})$	$\eta_{\text{MUX}}(\%/\text{W}^2)$
8	7.4	8.0	-29	157

Table 4.4: Numerical example of a practical MUX design with reduced data channel spacing and higher efficiency. Efficiency calculated with 3-dB loss.

Several issues still accompany the proof-of-principle device. Although the residual pump pulse falls between two signal pulses, it is better further attenuated (ideally 25 dB more) before true system tests are carried out. Cascading multiple ω-removers may solve this problem, as each one can provide $10-20$ dB for pump attenuation. Using a combination of other types of ω-removers, e.g. a tight bend that radiates the FH but transmits the SH light, or a narrow waveguide that cutoff the FH light, is also likely to help. The loss of the deep exchange waveguides is roughly 0.4 dB/cm, at both FH and SH wavelengths, compared to 0.1 dB/cm for conventional RPE waveguides. Ideally, the MUX would be fabricated on a 4-inch-diameter wafer so that the tight U-turn bend would not be necessary and conventional RPE waveguides could be used. Finally, with high average clock power, the generated SH light can be harmful to the waveguides. Waveguides fabricated on photorefractive-resistant materials, e.g. stoichiometric or Mg-doped lithium niobate and lithium tantalate, [27, 67, 68] may ultimately solve this problem.

Chapter 5

Conclusion

5.1 Summary of Contributions

The essential contribution of this dissertation is to extend the functionality of PPLN-based optical signal-processing devices.

We addressed the bandwidth/efficiency trade-off of OF mixers in Chapter 2 by introducing a quasi-group-velocity-matched structure. With the QGVM technique, one no longer has to trade efficiency for high bit-rate in bit-level optical signal processing. QGVM is not only analogous but also complementary to the now mature quasi-phase(-velocity-)matching technique. The two, together with grating-period chirping to accommodate GVD, allow us to effectively manipulate the zeroth- through second-order dispersion of short optical pulses.

To further lift the constraint on optical signal processors, in Chapter 3 we developed several techniques to modulate the nonlinear interaction amplitude. These techniques proved successful to suppress transfer-function sidelobes and thereby minimize interchannel crosstalk in optical communication systems. Combined with other QPM engineering techniques, e.g. domain-phase modulation and dispersion manipulation, amplitude modulation is a big step forward toward truly versatile spectral shaping of optical pulses.

These techniques are compatible with, indeed based on, integrated optical circuits. We added to that toolbox a 2-mm-radius U-turn bend based on deep exchange RPE

waveguides. It allowed for doubled device length and the integration of more signal-processing functions on a single chip.

The latest effort in optical signal processing has been to go beyond discrete signal-processing functions and build integrated multifunctional devices. Chapter 4 of this dissertation demonstrated a sophisticated optical signal-processing device: a monolithic OTDM-MUX capable of 160-Gbit/s operation. Its integrated operation could not be successful without a toolkit of individual signal-processing functions, the ability to tailor them by design, and to integrate them with strict grating- and waveguide-fabrication requirements. Besides the advantages of being monolithic, the demonstrated device had figures of merit that met or exceeded previously demonstrated MUXs.

5.2   Future Directions

Many new directions for optical signal processing in PPLN have been outlined in individual chapters. Once the basic building blocks are available, e.g. OF mixers and waveguide structures, many of the developments in this dissertation can be extended to other material systems. Orientation-patterned semiconductors such as GaAs have higher nonlinear coefficients and can operation in polarization independent fashion, making them attractive for optical signal processing.

The single most severe problem for current devices is the photorefractive damage. At high power levels, RPE waveguides fabricated on congruent lithium niobate are slowly damaged by green or blue light generated by parasitic SHG or SFG processes even if the chips are heated to 150 °C. An important direction is to improve periodic poling and develop low-loss waveguides in photorefractive-damage resistant materials, such as MgO-doped or stoichiometric lithium niobate and lithium tantalate. [27, 67, 68]

On the device side, the tight circular bend made possible on-chip optical loops and cavities. If the propagation loss is further reduced, devices based on those concepts could be designed. Another possibility is to develop other U-turn structures, for example a half-length directional coupler with a high-reflection-coated end facet.

This structure is compatible with the low-loss conventional RPE waveguides but will require higher fabrication precision.

Next-generation devices may also combine nonlinear optical and electro-optical functions. MQGVM devices may perform better by adding EO phase shifters in each QGVM section and synchronizing their phase relations. Applying opposite voltages to the reversed domains would allow us to tune the QPM wavelength after the chip is made, over a range not achievable by temperature tuning. The fabrication process would require one extra lithography step for aligning electrodes with the gratings and waveguides.

Appendix A

Tuning Behavior in Non-ideal Waveguides

The SHG tuning curve is a good diagnostic for optical signal-processing devices. In real devices, various distortions to the tuning curve result from fabrication errors. (Figure A.1) Around the center of the phasematching peak, reduced peak height is often accompanied by asymmetric/broadened/enhanced sidelobes. Far off phasematching, sidelobe heights deviate from the theoretical curve, and a floor of roughly $1/N$ (N is the number of QPM periods) was observed. (see Chapter 3)
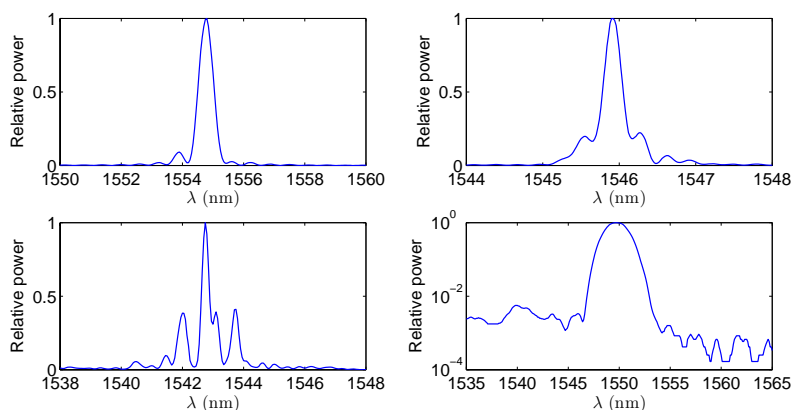

Figure A.1: Examples of tuning curve distortion in four different experimental devices.

For many applications, distortion of the tuning curve is often more serious than

reduced peak efficiency. In optical communication devices, broadened peaks and enhanced sidelobes may cause interchannel crosstalk. The $1/N$-floor of the transfer function is responsible for photons generated by parametric fluorescence far from phasematching, a problem in photon-counting experiments. [69] With high optical power, those photons generated by non-phasematched SHG can also alter, temporarily or permanently, the properties of waveguides through photorefractive processes.

These effects originate from two main categories of fabrication errors: perturbations to the waveguide and to QPM domain boundaries. In-depth study has been carried out on QPM domain boundary errors. [16] This appendix presents a theoretical study of deterministic and random perturbations to waveguides and their impact on tuning curve shapes. Although we restrict the examples to SHG, it can be readily extended to the cases of other nonlinear interactions.

A.1   Methodology

Starting from the formal solutions of the coupled-mode equations in the low conversion limit, the tuning curve of a device with spatially varying phase mismatch, normalized to that of an ideal device of the same length L, $|g(\Omega)|^2$, can be calculated by [16]

$$|g(\Omega)|^2 = |\frac{1}{L} \int_0^L e^{i\Delta\phi(z,\Omega)} \, dz|^2 \qquad (A.1)$$

$$\Delta\phi(z,\Omega) = \int_0^z \Delta\beta(z',\Omega) \, dz', \qquad (A.2)$$

where Ω is the detuning from a reference frequency ω_0, L is the length of the device and $\Delta\beta(z,\Omega) = \beta(z,\omega_0 + \Omega) - 2\beta(z,\omega_0/2 + \Omega/2) - k_g$, where k_g is the grating k-vector, is the effective wavevector mismatch between the interacting waves. In order to calculate $g(\Omega)$ it is necessary to specify the form of $\Delta\beta(z,\Omega)$, and hence $\Delta\phi(z,\Omega)$. The simplest form of $\Delta\beta(z,\Omega)$ is independent of z. In this case, the integral for $g(\Omega)$ is trivial, resulting in $g(\Omega) = e^{i\Delta\beta L/2}\text{sinc}[\Delta\beta(\Omega)L/2]$, reproducing the well known result for phasematching in a homogeneous medium or with a uniform QPM grating. We shall later examine devices with specified forms of $\Delta\beta(z,\Omega)$ of practical or illustrative

importance.

$\Delta\beta$ can be expanded in a Taylor series in δw, the deviation of the waveguide width from its nominal value w. When $\Delta\beta$ has a first order dependence on δw, the phasematching can be considered critical, whereas when $\Delta\beta$ has only a second order dependence on δw, the phasematching is considered noncritical. [25, 27] In our analysis below we distinguish perturbations to these two different types of waveguides.

We also provide numerical examples in the context of PPLN devices. The "error-free" prototype is a RPE PPLN waveguide that has a uniform QPM period of 16 μm, 625 periods (1-cm long), and either a 5-μm critical width or 8-μm noncritical width. For deterministic perturbations, we relate the theoretical results to measurable parameters (waveguide width, exchange dose, QPM wavelength, etc.) using a 2-dimensional waveguide model. [27] For random perturbations, we generate an actual device by introducing random errors in local wavevector mismatch, $\Delta\beta$, and simulate its tuning curve rigorously by tracking the phase of the SH wave generated by each QPM domain and summing those waves at the output. We also numerically calculate the averaged performance of the randomly perturbed waveguide ensemble.

A.2   Systematic Perturbations

Linear taper

The prototypical systematic perturbation is a linear variation in $\Delta\beta$ with respect to z:

$$\Delta\beta(z, \Omega) = \delta\nu\Omega + \frac{\delta\beta_M}{L}\left(z - \frac{L}{2}\right), \tag{A.3}$$

where $\Omega = \omega - \omega_0$ is chosen such that at the center of the device $\Delta\beta(L/2, 0) = 0$, $\delta\nu$ is the GVM parameter, and $\delta\beta_M$ is the difference in $\Delta\beta$ from one end of the device to the other. The accumulated phase error is

$$\Delta\phi(z, \Omega) = \left(\delta\nu\Omega - \frac{\delta\beta_M}{2}\right)z + \frac{\delta\beta_M}{2L}z^2. \tag{A.4}$$

The tuning curve can be calculated with Eqs. (A.1) and (A.4), and expressed in

terms of Fresnel integrals $C(z)$ and $S(z)$,

$$|g(\Omega)|^2 = \frac{[C((1-\zeta)a) + C(\zeta a)]^2 + [S((1-\zeta)a) + S(\zeta a)]^2}{a^2}, \qquad (A.5)$$

where $a = \sqrt{\delta\beta_M L/\pi}$ and $\zeta = 1/2 - \delta\nu\Omega/\delta\beta_M$. The function is plotted in Figure A.2 for several values of $\delta\beta_M L$. The symmetric widening of the tuning curve is due to the fact that a band of frequencies are locally phasematched at different locations along the propagation direction, as a result of tapering. The effect is similar to that of a linearly chirped QPM grating.
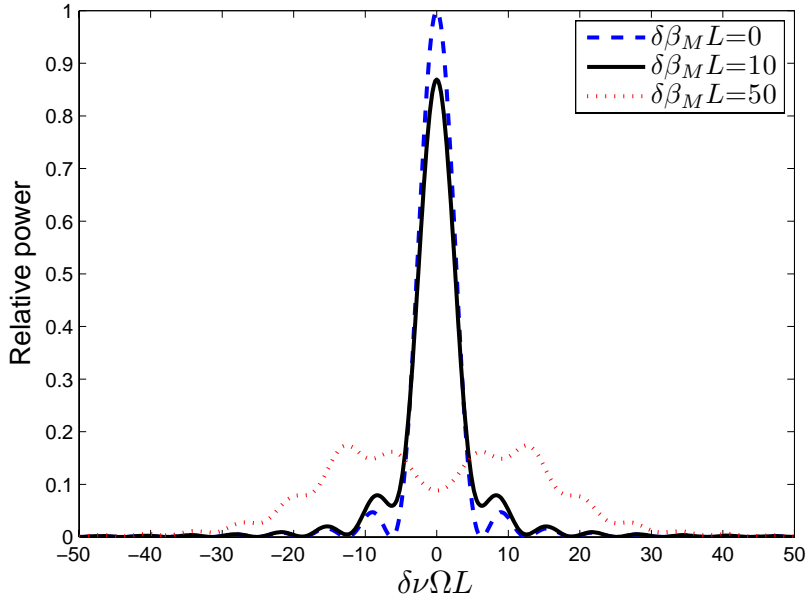
Figure A.2: Systematic perturbation: linear tapers.

A linear taper in $\Delta\beta$ can result from a waveguide mask with a linear width taper if the design is critical, or when a gradient of exchange dose, due to a temperature gradient in the exchange bath, for example, exists over the length of the waveguide. As there are different origins of errors, we quantify the magnitude of error by a shift in local phasematching wavelength $\delta\lambda_{\mathrm{QPM}}(z)$. In the above-mentioned prototype device, the perturbation $\Delta\beta_M L=10$ and 50 correspond to maximum $\delta\lambda_{\mathrm{QPM}}$ of ± 0.8

and ± 4 nm, respectively, at either end of the waveguide. If it is due to a width taper, it corresponds to width changes of ± 0.1 and ± 0.5 μm, respectively, at either end, around a critical width of 5 μm.

Quadratic taper

$\Delta\beta$ sometimes has the form of a quadratic taper with respect to z:

$$\Delta\beta(z,\Omega) = \delta\nu\Omega + \frac{2\delta\beta_M}{L^2}\left(z - \frac{L}{2}\right), \tag{A.6}$$

Again ω_0 is phasematched at the center of the device. The additional wavevector mismatch at both ends due to the taper is $\delta\beta_M/2$. So with Eq.(A.2)

$$\Delta\phi(z,\Omega) = \delta\nu\Omega z + \frac{2\delta\beta_M}{3L^2}\left(z - \frac{L}{2}\right)^3 + \frac{\delta\beta_M L}{12}. \tag{A.7}$$

Evaluation of the integral in Eq.(A.1) leads to an expression containing incomplete Gamma functions. The tuning curve is plotted in Figure A.3, with parameter $\delta\beta_M L$.
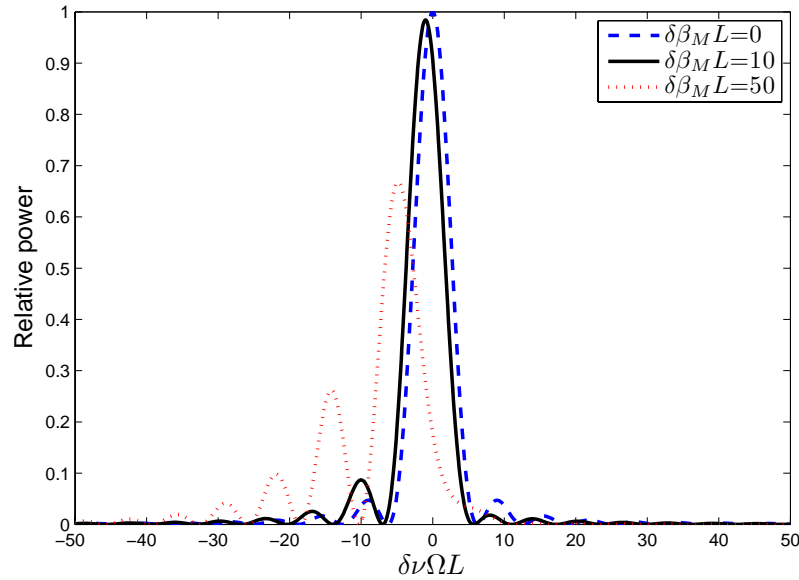
Figure A.3: Systemetic perturbation: quadratic tapers.

With an 8-μm noncritical waveguide width, any width change moves the wavevector mismatch toward one direction, and a quadratic taper in $\Delta\beta$ is a good approximation for a linear taper in waveguide width. In this case $\delta\lambda_{\text{QPM}}$=0.8 and 4 nm correspond to width changes of 1 and 3.2 μm, respectively, at either end. We see that at the noncritical point, the tolerances for dimensional errors are substantially increased. As the taper gets steeper, the tuning curve becomes more asymmetric and its peak shifted to one side, because a quadratic taper moves all local phasematching wavelengths toward one direction.

Periodic perturbation

Another interesting class of perturbations vary periodically in z. Prototypical of these is a sinusoidally varying wavevector error of the form

$$\Delta\beta(z, \Omega) = \delta\nu\Omega + \delta\beta_M \sin(K_\beta z). \tag{A.8}$$

The accumulated phase error is found to be

$$\Delta\phi(z, \Omega) = \delta\nu\Omega z + r[1 - \cos(K_\beta z)], \tag{A.9}$$

where $r \equiv \delta\beta_M/K_\beta$. The tuning curve takes the form

$$|g(\Omega)|^2 = \left| \frac{1}{K_\beta L} \int_0^{K_\beta L} e^{i\left[\frac{\delta\nu\Omega}{K_\beta}x - r\cos(x)\right]} dx \right|^2. \tag{A.10}$$

If we assume for simplicity that L is an integral multiple of the modulation half-period, i.e. $K_\beta L = m\pi$, and use standard integral representations of the Bessel functions, we obtain

$$|g(\Omega)|^2 = J^2_{\delta\nu\Omega/K_\beta}(r). \tag{A.11}$$

It is plotted in Figure A.4 with detuning and parameters m and $\delta\beta_M L$. In general, a periodic modulation splits the tuning curve. This is similar to the phase-modulated QPM gratings, where domain centers are shifted in a controlled manner to generate multiple phasematching peaks, and the shorter the modulation period, the larger the split. [49]

Figure A.4: Periodic perturbations. Top: a device contains 2 modulation half-periods; bottom: 20 modulation half-periods.

A.3   Random Perturbations
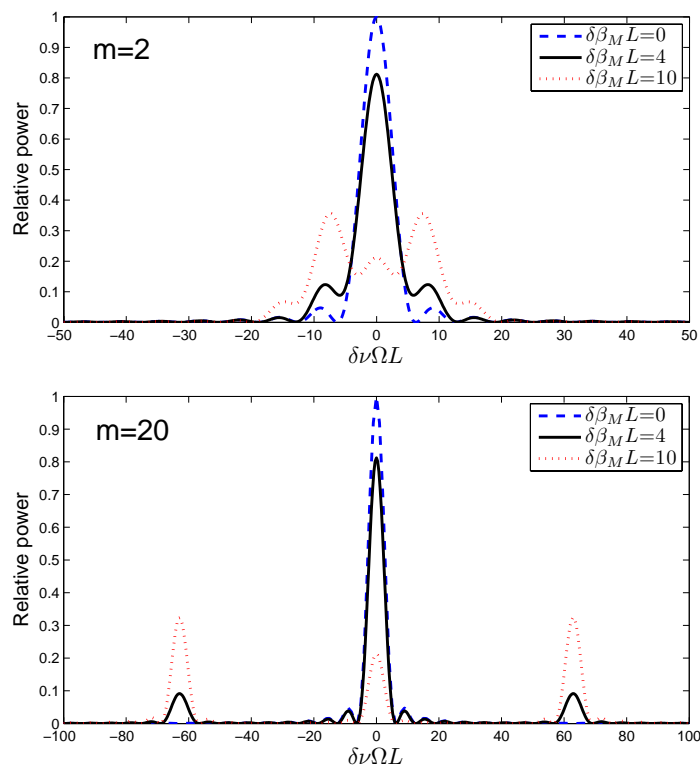
In many practical cases, we have only statistical information about the perturbations. In this section we study the tuning behavior in randomly perturbed waveguides, given only statistical information about $\Delta\beta$ along z. We choose the reference frequency ω_0 such that for this frequency, without random perturbations, the wavevector mismatch $\Delta\beta_0(\Omega = 0)$ is zero. We assume the z-dependent perturbation distribution is the same for all Ω, so we can use the simplified notations without the explicit argument Ω. The total wavevector mismatch is the sum of the effects of tuning ($\Delta\beta_0 = \delta\nu\Omega$) and random perturbation ($\Delta\beta_r(z)$), i.e. $\Delta\beta(z) = \Delta\beta_0 + \Delta\beta_r(z)$. Furthermore, we assume that $\Delta\beta_r(z)$ is stationary with respect to z, and has an autocorrelation length Λ small compared to L. Defining $\langle f \rangle$ as the mean value of a random function f and $\{f\}$ the ensemble average of f, we assume ergodicity so that $\langle f \rangle = \{f\}$. The analysis we apply here borrows heavily from the discussion of random QPM period error in Ref. [16].

We begin the analysis by deriving an expression for $|g|^2$ that is more convenient for statistical evaluation. With Eqs. (A.1) and (A.2) we have

$$|g|^2 = \left[\frac{1}{L}\int_0^L e^{i\Delta\phi(z)}\,dz\right]\left[\frac{1}{L}\int_0^L e^{-i\Delta\phi(z)}\,dz\right] = \frac{1}{L^2}\int_0^L dz \int_0^L e^{-i[\Delta\phi(z)-\Delta\phi(z')]}\,dz'. \tag{A.12}$$

Dividing the inner integral into two parts, $0 \leq z' \leq z$ and $z \leq z' \leq L$ and, for the first of these double integrals, reversing the order of integration and exchanging the dummy integration variables, and then recombining the two double integrals results in

$$|g|^2 = \frac{2}{L^2}\int_0^L dz \int_z^{L-z} \cos[\Delta\phi(z+z'') - \Delta\phi(z)]\,dz''. \tag{A.13}$$

To this point, we have simply reformulated an exact expression for $|g|^2$. Since we have only statistical information about the waveguide, we are interested in the ensemble average of $|g|^2$, which, with Eq.(A.13), is given by

$$\{|g|^2\} = \frac{2}{L^2}\int_0^L dz \int_z^{L-z} \{\cos[\Delta\phi(z+z'') - \Delta\phi(z)]\}\,dz''. \tag{A.14}$$

To make further progress, we must include information derived from the distribution function of $\Delta\beta_r(z)$. Since it is assumed stationary, the argument of the cosine may be replaced by $\Delta\phi(z'')$, and Eq.(A.14) becomes

$$\left\{|g|^2\right\} = \frac{2}{L^2} \int_0^L dz \int_z^{L-z} \left\{\cos[\Delta\phi(z'')]\right\} dz''. \tag{A.15}$$

To evaluate the ensemble average appearing in the integrand, we need to know $p[\Delta\phi(z)]$, the distribution function of $\Delta\phi(z)$.

For critical phasematching, $\Delta\beta_r(z) \propto \delta w(z)$, where $\delta w(z)$ is the random variation in waveguide width. If we assume that $\delta w(z)$ is normally distributed, $\Delta\beta_r(z)$ are as well, and $\overline{\Delta\beta_r}(z) = 0$. We can take $p[\Delta\phi(z)]$ to be

$$p[\Delta\phi(z)] = \frac{1}{\sqrt{2\pi}\sigma_\phi(z)} e^{-[\Delta\phi(z)-\overline{\Delta\phi}(z)]^2/2\sigma_\phi^2(z)}, \tag{A.16}$$

where $\overline{\Delta\phi}(z)$ and $\sigma_\phi(z)$ are the mean and the variance of $\Delta\phi(z)$, respectively. So

$$\left\{\cos[\Delta\phi(z)]\right\} = \int_{-\infty}^{\infty} p[\Delta\phi(z)] \cos[\Delta\phi(z)] \, d\Delta\phi(z) = e^{-\sigma_\phi^2(z)} \cos[\overline{\Delta\phi}(z)], \tag{A.17}$$

where the second form of Eq.(A.17) follows from the first with Eq.(A.16) and a standard definite integral. With Eq.(A.17), Eq.(A.15) takes the form

$$\left\{|g|^2\right\} = \frac{2}{L^2} \int_0^L dz \int_z^{L-z} e^{-\sigma_\phi^2(z'')/2} \cos[\overline{\Delta\phi}(z'')] \, dz''. \tag{A.18}$$

With Eq.(A.2) it is clear that

$$\overline{\Delta\phi}(z) = z\overline{\Delta\beta} = z\Delta\beta_0. \tag{A.19}$$

Calculation of $\sigma_\phi(z)$ is somewhat more involved. Define $\Delta\phi_r(z) \equiv \Delta\phi(z) - \overline{\Delta\phi}(z)$, so that the variance $\sigma_\phi(z)$ is given by

$$\sigma_\phi^2(z) = \left\{[\Delta\phi_r(z)]^2\right\}. \tag{A.20}$$

To evaluate Eq.(A.20), we ask what is the ensemble average of the square increment between z and $z + Z$. With Eq.(A.2), we have

$$
\begin{aligned}
\left\{ [\Delta\phi_r(z + Z) - \Delta\phi_r(z)]^2 \right\} &= \left\{ \left[\int_z^{z+Z} \left(\Delta\beta(z') - \overline{\Delta\beta} \right) dz' \right]^2 \right\} \\
&= \left\{ \left[\int_z^{z+Z} \Delta\beta_r(z') \, dz' \right]^2 \right\} \\
&= \int_z^{z+Z} dz' \int_z^{z+Z} \left\{ \Delta\beta_r(z') \Delta\beta_r(z'') \right\} dz''. \quad \text{(A.21)}
\end{aligned}
$$

Defining $s \equiv z'' - z'$, Eq.(A.21) can be written as

$$
\left\{ [\Delta\phi_r(z + Z) - \Delta\phi_r(z)]^2 \right\} = \int_z^{z+Z} dz' \int_{z-z'}^{z-z'+Z} B_r(s) \, ds, \quad \text{(A.22)}
$$

where the autocorrelation function $B_r(s)$, defined as

$$
B_r(s) = \left\{ \Delta\beta_r(z) \Delta\beta_r(z + s) \right\}, \quad \text{(A.23)}
$$

is independent of z if the statistics of $\Delta\beta_r(z)$ are stationary. To evaluate Eq.(A.22), divide the inner integral into two intervals, $z - z' \leq z'' \leq 0$ and $0 \leq z'' \leq z - z' + Z$, change the order of integration in both the resulting double integrals, to obtain

$$
\left\{ [\Delta\phi_r(z + Z) - \Delta\phi_r(z)]^2 \right\} = \int_{-Z}^{Z} (Z + s) B_r(s) \, ds \quad \text{(A.24)}
$$

As long as we are interested in increments Z long compared to the autocorrelation length Λ, we can use the property of the autocorrelation function that $B_r(s) \to 0$ for $s \gg \Lambda$ to neglect s with respect to Z over the entire range over which the integrand is appreciable, and to extend the limits of integration in Eq.(A.24) to $\pm\infty$. With these assumptions, Eq.(A.24) becomes

$$
\left\{ [\Delta\phi_r(z + Z) - \Delta\phi_r(z)]^2 \right\} = Z \int_{-\infty}^{\infty} B_r(s) \, ds. \quad \text{(A.25)}
$$

Noting that the RHS of Eq.(A.25) is independent of z, this result can be generalized

to write Eq.(A.20) as

$$\sigma_\phi^2(z) = z \int_{-\infty}^{\infty} B_r(s) \, ds. \tag{A.26}$$

From Eqs. (A.19) and (A.26), we see that both $\overline{\Delta\phi}(z)$ and $\sigma_\phi^2(z)$ grow linearly with z. For the following discussion, it is convenient to define a constant, Γ, such that

$$\Gamma = \frac{1}{\Lambda \langle \Delta\beta_r^2 \rangle} \int_{-\infty}^{\infty} B_r(s) \, ds. \tag{A.27}$$

This choice of normalization is based on two properties of the autocorrelation function, $B_r(s)$, i.e. that $B_r(0) = \{\Delta\beta_r^2\} = \sigma_{\Delta\beta}^2$ and that $B_r(s)$ has a characteristic width Λ, so that Γ is of order unity. Γ is not strongly dependent on the form assumed for the autocorrelation, as is seen below

$$B_r(s) = \sigma_{\Delta\beta}^2 \begin{pmatrix} \mathrm{rect}(s/\Lambda) \\ e^{-(s/\Lambda)^2} \\ e^{-|s|/\Lambda} \\ [1 + (s/\Lambda)^2]^{-1} \end{pmatrix} \Rightarrow \Gamma = \begin{pmatrix} 2 \\ \sqrt{\pi} \\ 2 \\ \pi \end{pmatrix} \tag{A.28}$$

We can cast Eq.(A.18) in the form

$$\begin{aligned} \{|g|^2\} &= \frac{2}{L^2} \int_0^L dz \int_z^{L-z} e^{-Sz''/L} \cos(Fz''/L) \, dz'' \\ &= 2D^{-2} \{F^2 - S^2 + SD + e^{-S} [(S^2 - F^2) \cos(F) - 2SF \sin(F)]\}, \end{aligned} \tag{A.29}$$

where

$$S = \frac{1}{2} \Gamma \Lambda L \sigma_{\Delta\beta}^2 \tag{A.30}$$

$$F = \overline{\Delta\beta} L = \delta\nu\Omega L \tag{A.31}$$

$$D^2 = F^2 + S^2 \tag{A.32}$$

$\{|g|^2\}$ is plotted in Figure A.5 as a function of detuning Ω for different values of S, a measure of disorder defined in Eq.(A.30). It should be noted that the tuning curve of a particular device chosen from an ensemble with given F and S does not necessarily resemble the ensemble average of the tuning curves. The breadth of the

ensemble average is in large part due to the distribution of peaks in the ensemble rather than the breadth of the tuning curve of individual elements in the ensemble, as the numerical examples in Figure A.6 show. Also note that the magnitude of the random error, $\sigma_{\Delta\beta}^2$, and the autocorrelation length Λ are interchangeable in the expression for S, so that large magnitude and long-range perturbations will have the same effect.
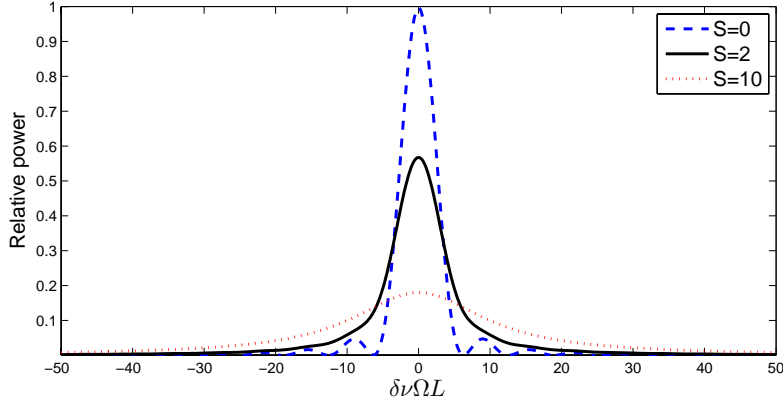
Figure A.5: The ensemble average of the tuning curves for SHG in waveguides with random perturbations. The parameter S, a measure of the magnitude of the perturbations, is defined in Eq.(A.30).

For noncritical phasematching, $\Delta\beta_r(z) \propto \delta w(z)^2$. This nonlinear relation causes a nonzero mean $\overline{\Delta\beta_r}(z)$ by "rectifying" the random function $\delta w(z)$. Now $\overline{\Delta\beta}(z) = \delta\nu\Omega + \overline{\Delta\beta_r}(z)$, manifesting a shift of the phasematching peak. It is difficult to make general statements about the variance and autocorrelation, as these involve fourth-order correlations of $\delta w(z)$. Furthermore, $\Delta\beta_r(z)$ and $\Delta\phi(z)$ are no longer normally distributed, so an analytical form of $\{|g|^2\}$ are not easy to obtain. Using the numerical method, we see that the perturbations shift the phasematching wavelengths to one side. (Figure A.7)

The perturbations randomly change the local phasematching wavelengths, so the center peak is distorted and broadened, whereas the effects on the tuning-curve wings are small. This is confirmed by Figure A.8.

Figure A.6: Numerical examples of random perturbation to a critically phasematched waveguide, assuming $\Lambda = 1$ mm, an autocorrelation function rect(s/Λ), and $S = 5$. The three individual curves (dashed) are from the ensemble with the same statistical properties. The theoretical (dotted, calculated using Eq.(A.29)) and numerical (solid, calculated by averaging 100 tuning curves from the same ensemble) ensemble average curves agree well.
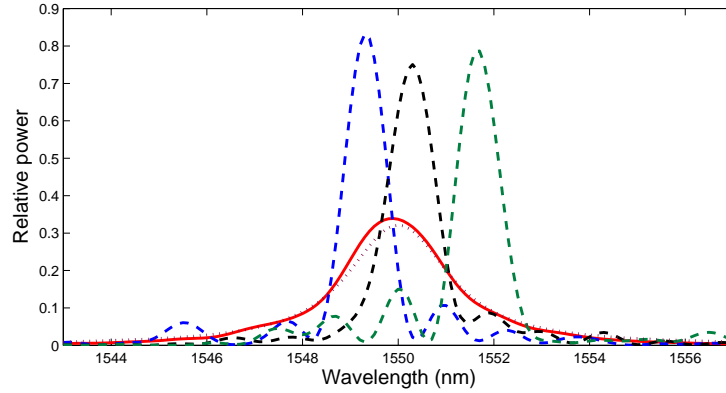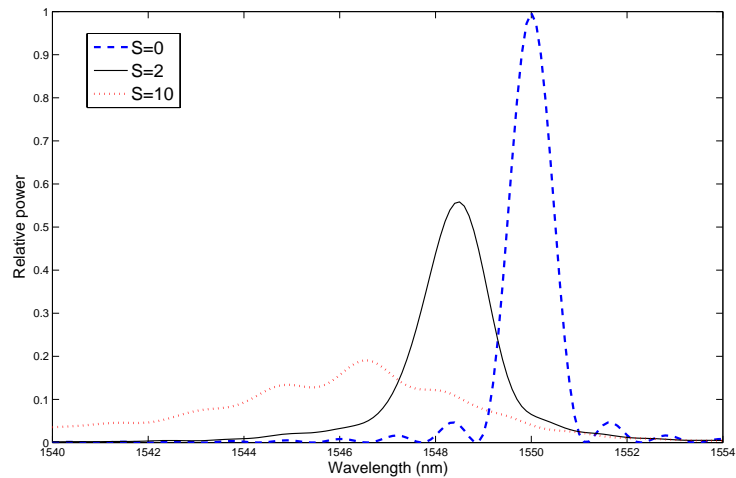

Figure A.7: Numerical examples of random perturbation to a noncritically phasematched waveguide, assuming $\Lambda = 1$ mm. The ensembles are calculated by averaging 100 curves with the same statistical properties.
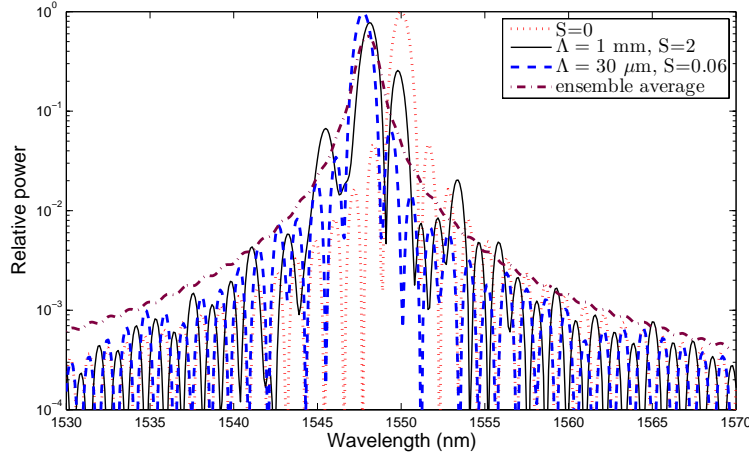
Figure A.8: Numerical examples of random perturbation to a noncritically phase-matched waveguide, with different autocorrelation lengths, holding $\sigma^2_{\Delta\beta}$ constant, together with the ensemble average of $S = 2$. Even when the magnitude of perturbation is large enough to clearly shift and distort the peaks around the phasematching center, the effect on the tuning-curve wings is small.

A.4   Summary

We have examined the effects of various departures from an ideal waveguide. The tuning properties were obtained analytically for each type of perturbation, i.e. linear and quadratic tapers, periodic modulation, and random waveguide errors. It is interesting to note that the effects of waveguide perturbations are most noticeable around the phasematching center, because in the expressions of both $\Delta\beta$ and $\Delta\phi$, with large enough detuning, the contribution of detuning dominates the contribution of perturbation. In other words, waveguide perturbations are mostly responsible for near-phasematching tuning-curve distortion, rather than off-phasematching photon generation. The latter is discussed in Appendix B.

Appendix B

Off-phasematching Photon Generation in QPM Gratings with Random Duty-cycle Errors

At least two types of random perturbation are of interest to a QPM grating. If a collection of plates of varying thickness are stacked to form the structure, the error in the position of the kth boundary is the sum of the errors in the thickness of all the previous layers, so that the errors grow with k in the manner of a random walk. This is called random period error. We note its similarity with random waveguide perturbations described in Appendix A. In both cases, the phase errors accumulate along the propagation direction, and the same statistical approach applies.

With the commonly used periodic-poling technique, however, QPM domains are defined by a photolithographic mask, which maintains the average position of the boundaries with uniform accuracy across the device, but local effects randomly perturb the position of each boundary, so the probable error in the kth boundary is independent of k. We refer to this type of structure as having a random duty-cycle error. In the context of lithographically patterned PPLN devices, only the random-duty-cycle error is of practical interest to us, since the long-range order is precisely controlled by the lithographic mask.

Both types of errors are studied in-depth in Ref. [16]. Instead of being a stand-alone study, this short appendix extends the results in the above reference to analyze off-phasematching photon generation in the context of random duty-cycle errors. The cited numbered equations all refer to those in Ref. [16].

Considering an error-free prototype device with N periods and the ith boundary at position $z_{i,0}$, and an actual device with variance of domain length σ_Λ^2, We calculate the efficiency of the actual device normalized to the peak efficiency of the ideal device $|g|^2 \equiv \eta/\eta_{\text{ideal}}$. According to Eq.(56),

$$\left\{|g|^2\right\} = \frac{1}{N} + \frac{2}{N^2} \sum_{k=1}^{N-1} \sum_{p=1}^{N-k} \{\cos(\Delta\Phi_{k,p})\}, \tag{B.1}$$

where $\Delta\Phi_{k,p} \equiv \Phi_{k+p} - \Phi_k$ is the phase error accumulated between layers k and $k+p$. For duty cycle errors, the errors in the boundary positions have zero mean and are independent and stationary with respect to k. Eq.(63) shows that the mean and variance of $\Delta\Phi_{k,p}$ are

$$\{\Delta\Phi_{k,p}\} = \delta\Delta k(z_{k+p,0} - z_{k,0}) = px \tag{B.2}$$

$$\sigma_\phi^2 \equiv \sigma_{\Delta\Phi_{k,0}} = \Delta k_0^2 \sigma_\Lambda^2, \tag{B.3}$$

where $\Delta k_0 \equiv \pi/L_c$ is the wavevector mismatch at the design wavelength, $\delta\Delta k = \delta\nu\Omega$ is the additional mismatch due to frequency detuning Ω, and $x \equiv \delta\Delta k m\Lambda$ with m being the order of phasematching. The independence of statistical quantities on k, due to the stationary assumption, allows us to drop the subscript k and use a simpler notation. For normally distributed errors, Eq.(65) shows

$$\{\cos(\Delta\Phi_{k,p})\} = e^{-\sigma_\phi^2/2} \cos(\{\Delta\Phi_p\}). \tag{B.4}$$

With the above equations we have

$$\left\{|g|^2\right\} = \frac{1}{N} + \frac{2}{N^2} e^{-\sigma_\phi^2/2} \sum_{k=1}^{N-1} \sum_{p=1}^{N-k} \{\cos(px)\}$$

$$\begin{aligned}
&= \frac{1}{N} + \frac{2}{N^2} e^{-\sigma_\phi^2/2} \sum_{k=1}^{N-1} \frac{e^{ix}}{e^{ix}-1} \left[e^{i(N-k)x} - 1 \right] \\
&= \frac{1}{N} \left(1 - e^{-\sigma_\phi^2/2} \right) + e^{-\sigma_\phi^2/2} \frac{\sin^2(Nx/2)}{N^2 \sin^2(x/2)},
\end{aligned} \tag{B.5}$$

where the second form follows from the first by rewriting the cosine as the sum of exponentials and summing a geometrical series, and the last is from long yet straightforward algebra. In the error-free limit, $\{|g|^2\} \rightarrow \frac{\sin^2(Nx/2)}{N^2 \sin^2(x/2)}$. It is not exactly a sinc-square known for a uniform grating, but the mth peak of the numerator is at $x = 2\pi(m+1/2)/N << 1$ for $N >> m$, so the denominator is close enough to $(Nx/2)^2$, and to good accuracy over the range of interest $\{|g|^2\} \approx \text{sinc}^2(Nx/2)$. On the other hand, with large random error, $\sigma_\phi >> 1$, we have $\{|g|^2\} \rightarrow 1/N$. (This is because with large random error the device works like the incoherent sum of N domains, and η scales with N, while η_{ideal} of the error-free grating scales with N^2.) It is most interesting to look at the practical case where σ_ϕ is between the two limits. Near the phasematching peak, the second term dominates with a peak height reduced by $e^{-\sigma_\phi^2/2}$, while with large detuning, the first term dominates, and the tuning curve exhibits a floor of the order $1/N$, regardless of tuning. We can also see from Eq.(B.5) and the definition of x that no matter how small σ_ϕ is, with large enough detuning, the first term will eventually dominate: a smaller random error pushes the floor further from the phasematching center. In contrast to the effects of waveguide perturbations discussed in Appendix A, random duty-cycle error has a most noticeable effect on off-phasematching photon generation. A numerical example and theoretical calculation are compared in Figure B.1.

A last note is on the validity of Eq.(32), which is the underlying assumption of Eq.(B.1). It assumes the quadratic term of phase error, $\delta\Delta k \delta z$, where δz is the domain boundary error, is small compared to π. For a typical C-band PPLN device with σ_Λ as large as 1.5 μm, the above assumption is valid over a tuning bandwidth of more than 1000 nm.
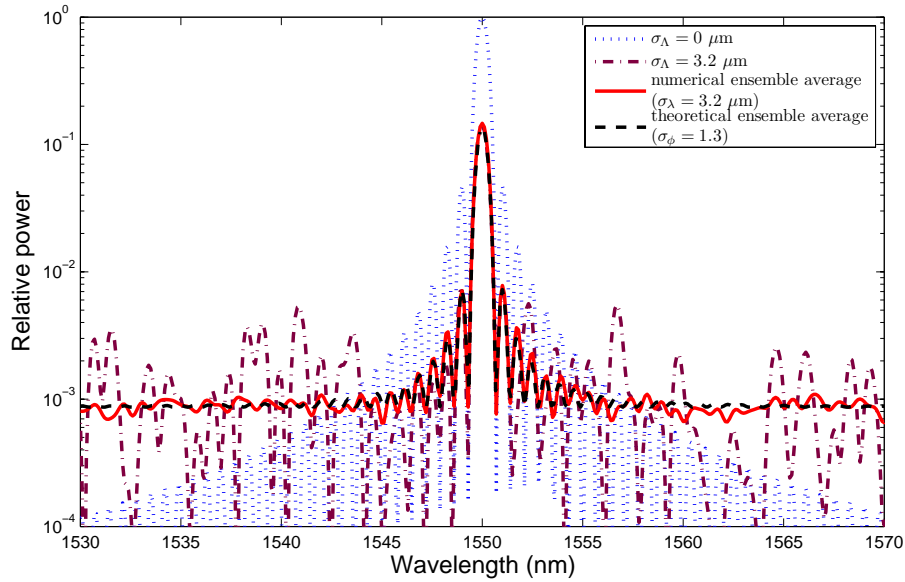
Figure B.1: Numerically calculated tuning curve for a specific example of randomly perturbed QPM devices compared to an ideal QPM device. The device has 1000 domains, and randomness characterized by the parameter σ_Λ. In addition, the ensemble average calculated using Eq.(B.5) with $\sigma_\phi = 1.3$ is compared to the average of 100 curves of $\sigma_\Lambda = 3.2$ μm. (Assuming a 15-μm QPM period, according to Eq.(B.3) the above σ_ϕ and σ_Λ are equivalent.)

Bibliography

[1] S. Kawanishi, H. Takara, K. Uchiyama, I. Shake, and K. Mori, "3 Tbit/s (160 Gbit/s× 19 channel) optical TDM and WDM transmission experiment," Electronics Letters **35**, 826–827 (1999).

[2] K. Parameswaran, R. Route, J. Kurz, R. Roussev, M. Fejer, and M. Fujimura, "Highly efficient second-harmonic generation in buried waveguides formed by annealed and reverse proton exchange in periodically poled lithium niobate," Optics Letters **27**, 179–181 (2002).

[3] M. Chou, "Optical frequency mixers using three-wave mixing for optical fiber communications," Ph.D. thesis, Stanford University (1999).

[4] C. Langrock, S. Kumar, J. McGeehan, A. Willner, and M. Fejer, "All-optical signal processing using $\chi(2)$ nonlinearities in guided-wave devices," Journal of Lightwave Technology **24**, 2579 (2006).

[5] C. Xu, H. Okayama, K. Shinozaki, K. Watanabe, and M. Kawahara, "Wavelength conversions ~1.5 μm by difference frequency generation in periodically domain-inverted LiNbO," Applied Physics Letters **63**, 1170–1172 (2006).

[6] M. Chou, I. Brener, M. Fejer, E. Chaban, and S. Christman, "1.5-μm-band wavelength conversion based on cascaded second-order nonlinearity in LiNbO$_3$ waveguides," IEEE Photonics Technology Letters **11**, 653–655 (1999).

[7] M. Chou, K. Parameswaran, M. Fejer, and I. Brener, "Multiple-channel wavelength conversion by use of engineered quasi-phase-matching structures in LiNbO$_3$ waveguides," Optics Letters **24**, 1157–1159 (1999).

[8] M. Chou, I. Brener, G. Lenz, R. Scotti, E. Chaban, J. Shmulovich, D. Philen, S. Kosinski, K. Parameswaran, and M. Fejer, "Efficient wide-band and tunable midspan spectral inverter using cascaded nonlinearities in LiNbO$_3$ waveguides," IEEE Photonics Technology Letters **12**, 82–84 (2000).

[9] S. Jansen, D. van den Borne, B. Spinnler, S. Calabro, H. Suche, P. Krummrich, W. Sohler, G. Khoe, and H. de Waardt, "Optical phase conjugation for ultra long-haul phase-shift-keyed transmission," Journal of Lightwave Technology **24**, 54–64 (2006).

[10] G. Imeshev, M. Arbore, M. Fejer, A. Galvanauskas, M. Fermann, and D. Harter, "Ultrashort-pulse second-harmonic generation with longitudinally nonuniform quasi-phase-matching gratings: pulse compression and shaping," Journal of the Optical Society of America B **17**, 304–318 (2000).

[11] S. Kawanishi, T. Yamamoto, M. Nakazawa, and M. Fejer, "High sensitivity waveform measurement with optical sampling using quasi-phasematched mixing in LiNbO$_3$ waveguide," Electronics Letters **37**, 842–844 (2001).

[12] H. Ishizuki, M. Fujimura, T. Suhara, and H. Nishihara, "LiNbO$_3$ waveguide quasi-phase-matched sum-frequency generation device for high-efficiency optical sampling," Electronics and Communications in Japan, Part 2 (Electronics) **84**, 29 – 36 (2001).

[13] K. Parameswaran, M. Fujimura, M. Chou, and M. Fejer, "Low-power all-optical gate based on sum frequency mixing in APE waveguides in PPLN," IEEE Photonics Technology Letters **12**, 654–656 (2000).

[14] M. Cardakli, D. Gurkan, S. Havstad, A. Willner, K. Parameswaran, M. Fejer, and I. Brener, "Tunable all-optical time-slot-interchange and wavelength conversion using difference-frequency-generation and optical buffers," IEEE Photonics Technology Letters **14** (2002).

[15] J. McGeehan, M. Hauer, A. Sahin, and A. Willner, "Multiwavelength-channel header recognition for reconfigurable WDM networks using optical correlators

based on sampled fiber Bragg gratings," IEEE Photonics Technology Letters **15**, 1464–1466 (2003).

[16] M. Fejer, G. Magel, D. Jundt, and R. Byer, "Quasi-phase-matched second harmonic generation: Tuning and tolerances," IEEE Journal of Quantum Electronics **28**, 2631–2654 (1992).

[17] S. Kawanishi, "Ultrahigh-speed optical time-division-multiplexed transmission technology based on optical signal processing," IEEE Journal of Quantum Electronics **34**, 2064–2079 (1998).

[18] T. Ohara, H. Takara, I. Shake, K. Mori, K. Sato, S. Kawanishi, S. Mino, T. Yamada, M. Ishii, I. Ogawa, T. Kitoh, K. Magari, M. Okamoto, R. Roussev, J. Kurz, K. Parameswaran, and M. Fejer, "160-Gb/s OTDM transmission using integrated all-optical MUX/DEMUX with all-channel modulation and demultiplexing," IEEE Photonics Technology Letters **16**, 650–652 (2004).

[19] T. Ohara, H. Takara, I. Shake, K. Mori, S. Kawanishi, S. Mino, T. Yamada, M. Ishii, T. Kitoh, T. Kitagawa, K. Parameswaran, and M. Fejer, "160-Gb/s optical-time-division multiplexing with PPLN hybrid integrated planar lightwave circuit," IEEE Photonics Technology Letters **15** (2003).

[20] G. Imeshev, "Tailoring of ultrafast frequency conversion with quasi-phase-matching gratings," Ph.D. thesis, Stanford University (2000).

[21] M. Arbore, "Generation and manipulation of infrared light using quasi-phasematched devices: ultrashort-pulse, aperiodic-grating and guided-wave frequency conversion," Ph.D. thesis, Stanford University (1998).

[22] J. Kurz, "Integrated Optical-frequency Mixers," Ph.D. thesis, Stanford University (2003).

[23] G. Imeshev, M. Fejer, A. Galvanauskas, and D. Harter, "Pulse shaping by difference-frequency mixing with quasi-phase-matching gratings," Journal of the Optical Society of America B **18**, 534–539 (2001).

[24] G. Miller, "Periodically poled lithium niobate: modeling, fabrication, and nonlinear-optical performance," Ph.D. thesis, Stanford University (1998).

[25] M. Bortz, S. Field, M. Fejer, D. Nam, R. Waarts, and D. Welch, "Noncritical quasi-phase-matched second harmonic generation in an annealed proton-exchanged LiNbO$_3$ waveguide," IEEE Journal of Quantum Electronics **30**, 2953–2960 (1994).

[26] E. Lim, "Quasi-Phasematching for guided-wave nonlinear optics in lithium niobate," Ph.D. thesis, Stanford University (1992).

[27] R. Roussev, "Optical-frequency mixers in periodically poled lithium niobate: materials, modeling and characterization," Ph.D. thesis, Stanford University (2006).

[28] M. Bortz and M. Fejer, "Annealed proton-exchanged LiNbO$_3$ waveguides," Optics Letters **16**, 1844–1846 (1991).

[29] H. Nishihara, M. Haruna, and T. Suhara, *Optical integrated circuits* (McGraw-Hill Professional, 1989).

[30] *Personal communication with Carsten Langrock.*

[31] J. Kurz, J. Huang, X. Xie, T. Saida, and M. Fejer, "Mode multiplexing in optical frequency mixers," Optics Letters **29**, 551–553 (2004).

[32] X. Xie and M. Fejer, "Two-spatial-mode parametric amplifier in lithium niobate waveguides with asymmetric Y junctions," Optics Letters **31**, 799–801 (2006).

[33] J. Kurz, X. Xie, C. Langrock, D. Hum, and M. Fejer, "Mode converters and sorters for quasi-phasematching waveguide devices," Lasers and Electro-Optics, 2003. CLEO'03. Conference on p. 2 (2003).

[34] X. Xie, T. Saida, J. Huang, and M. Fejer, "Shape optimization of asymmetric Y-junction for mode multiplexing in proton-exchange lithium niobate waveguides," Proceedings of SPIE **5728**, 360 (2005).

[35] Y. Fukuchi, T. Sakamoto, K. Taira, K. Kikuchi, D. Kunimatsu, A. Suzuki, and H. Ito, "Speed limit of all-optical gate switches using cascaded second-order nonlinear effect in quasi-phase-matched LiNbO$_3$ devices," IEEE Photonics Technology Letters **14**, 1267–1269 (2002).

[36] X. Xie, J. Huang, and M. Fejer, "Narrow-linewidth near-degenerate optical parametric generation achieved with quasi-group-velocity-matching in lithium niobate waveguides," Optics Letters **31**, 2190–2192 (2006).

[37] M. Webb, D. Eimerl, and S. Velsko, "Wavelength insensitive phase-matched second-harmonic generation in partially deuterated KDP," Journal of the Optical Society of America B **9**, 1118–1127 (1992).

[38] K. Hayata and M. Koshiba, "Group-velocity-matched second-harmonic generation: an efficient scheme for femtosecond ultraviolet pulse generation in periodically domain-inverted β-BaB," Applied Physics Letters **62**, 2188–2190 (2006).

[39] N. Yu, J. Ro, M. Cha, S. Kurimura, and T. Taira, "Broadband quasi-phase-matched second-harmonic generation in MgO-doped periodically poled LiNbO$_3$ at the communications band," Optics Letters **27**, 1046–1048 (2002).

[40] D. Jundt, "Temperature-dependent Sellmeier equation for the index of refraction, ne, in congruent lithium niobate," Optics Letters **22**, 1535–1555 (1997).

[41] A. Schober, M. Charbonneau-Lefort, and M. Fejer, "Broadband quasi-phase-matched second-harmonic generation of ultrashort optical pulses with spectral angular dispersion," Journal of the Optical Society of America B **22**, 1699–1713 (2005).

[42] M. Abramowitz and I. Stegun, *Handbook of mathematical functions, with formulas, graphs, and mathematical tables* (Dover Publications, 1965).

[43] J. Ranka, A. Gaeta, A. Baltuska, M. Pshenichnikov, and D. Wiersma, "Autocorrelation measurement of 6-fs pulses based on the two-photon-induced photocurrent in a GaAsP photodiode," Optics Letters **22**, 1344–1346 (1997).

[44] M. Taya, M. Bashaw, and M. Fejer, "Photorefractive effects in periodically poled ferroelectrics," Optics Letters **21**, 857–859 (1996).

[45] G. Agrawal, *Nonlinear fiber optics* (Academic Press, 2001).

[46] P. Loza-Alvarez, M. Ebrahimzadeh, W. Sibbett, D. Reid, D. Artigas, and M. Missey, "Femtosecond second-harmonic pulse compression in aperiodically poled lithium niobate: a systematic comparison of experiment and theory," Journal of the Optical Society of America B **18**, 1212–1217 (2001).

[47] J. Kurz, A. Schober, D. Hum, A. Saltzman, and M. Fejer, "Nonlinear physical optics with transversely patterned quasi-phase-matching gratings," IEEE Journal of Selected Topics in Quantum Electronics **8** (2002).

[48] J. Kurz, X. Xie, and M. Fejer, "Odd waveguide mode quasi-phase matching with angled and staggered gratings," Optics Letters **27**, 1445–1447 (2002).

[49] M. Asobe, O. Tadanaga, H. Miyazawa, Y. Nishida, and H. Suzuki, "Multiple quasi-phase-matched $LiNbO_3$ wavelength converter with a continuously phase-modulated domain structure," Optics Letters **28**, 558–560 (2003).

[50] Y. Lee, F. Fan, Y. Huang, B. Gu, B. Dong, and M. Chou, "Nonlinear multiwavelength conversion based on an aperiodic optical superlattice in lithium niobate," Optics Letters **27**, 2191–2193 (2002).

[51] T. Kartaloglu, Z. Figen, and O. Aytür, "Simultaneous phase matching of optical parametric oscillation and second-harmonic generation in aperiodically poled lithium niobate," Journal of the Optical Society of America B **20**, 343–350 (2003).

[52] A. Zverev, *Handbook of filter synthesis* (Wiley New York, 1967).

[53] H. Takahashi, K. Oda, and H. Toba, "Impact of crosstalk in an arrayed-waveguide multiplexer on N×N optical interconnection," Journal of Lightwave Technology **14**, 1097–1105 (1996).

[54] G. Agrawal, *Fiber-optic communication systems* (Wiley-Interscience, 2002).

[55] I. Monroy, E. Tangdiongga, R. Jonker, and H. de Waardt, "Interferometric crosstalk reduction by phase scrambling," Journal of Lightwave Technology **18**, 637–646 (2000).

[56] *Acceptable crosstalk level depends on its mechanism and number of channels of the system. For in-band crosstalk and when signal phase scrambling is possible, the maximum acceptable crosstalk is -20 dB. A stricter requirement applies when signal phase scrambling is not available. See Ref. [54, 55]* .

[57] H. Schnopper and R. Thompson, "Fourier spectrometers," Methods of Experimental Physics 12A: Astrophysics .

[58] E. Weisstein, *Apodization function* (http://mathworld.wolfram.com).

[59] D. Johns and K. Martin, *Analog integrated circuit design* (John Wiley & Sons New York, 1997).

[60] S. Yang, A. Weiner, K. Parameswaran, and M. Fejer, "400-photon-per-pulse ultrashort pulse autocorrelation measurement with aperiodically poled lithium niobate waveguides at 1.55 μm," Optics Letters **29**, 2070–2072 (2004).

[61] S. Yang, A. Weiner, K. Parameswaran, and M. Fejer, "Ultrasensitive second-harmonic generation frequency-resolved optical gating by aperiodically poled LiNbO3 waveguides at 1.5 μm," Optics Letters **30**, 2164–2166 (2005).

[62] C. Langrock, "Classical and low-light-level detection and pulse characterization using optical-frequency mixers," Ph.D. thesis, Stanford University (2007).

[63] M. Jinno, "Effects of crosstalk and timing jitter on all-optical time-divisiondemultiplexing using a nonlinear fiber Sagnac interferometer switch," IEEE Journal of Quantum Electronics **30**, 2842–2853 (1994).

[64] X. Xie and M. Fejer, "Cascaded optical parametric generation in reverse-proton-exchange," Optics Letters **28**, 558–560 (2003).

[65] J. Huang, J. Kurz, C. Langrock, A. Schober, and M. Fejer, "Quasi-group-velocity matching using integrated-optic structures," Optics Letters **29**, 2482–2484 (2004).

[66] A. Yariv, H. Blauvelt, D. Huff, and H. Zarem, "An experimental and theoretical study of the suppression of interferometric noise and distortion in AM optical links by phase dither," Journal of Lightwave Technology **15**, 437 (1997).

[67] D. Hum, "Frequency conversion in near-stoichiometric lithium tantalate fabricated by vapor transport equilibration," Ph.D. thesis, Stanford University (2007).

[68] M. Katz, R. Route, D. Hum, K. Parameswaran, G. Miller, and M. Fejer, "Vapor-transport equilibrated near-stoichiometric lithium tantalate for frequency-conversion applications," Optics Letters **29**, 1775–1777 (2004).

[69] C. Langrock, E. Diamanti, R. Roussev, Y. Yamamoto, M. Fejer, and H. Takesue, "Highly efficient single-photon detection at communication wavelengths by use of upconversion in reverse-proton-exchanged periodically poled $LiNbO_3$ waveguides," Optics Letters **30**, 1725–1727 (2005).